Fall 2016

Environmental Drivers of Benthic-Interior Exchange Events Over the Continental Shelf of Monterey Bay, California

Ben Yair Raanan
San Jose State University

ENVIRONMENTAL DRIVERS OF BENTHIC-INTERIOR EXCHANGE EVENTS OVER THE CONTINENTAL SHELF OF MONTEREY BAY, CALIFORNIA

A Thesis

Presented to

The Faculty of Moss Landing Marine Laboratories

San José State University

In Partial Fulfillment

of the Requirements for the Degree

Master of Science

by

Ben Yair Raanan

December 2016

The Designated Thesis Committee Approves the Thesis Titled

ENVIRONMENTAL DRIVERS OF BENTHIC-INTERIOR EXCHANGE EVENTS OVER THE CONTINENTAL SHELF OF MONTEREY BAY, CALIFORNIA

by

Ben Yair Raanan

APPROVED FOR THE DEPARTMENT OF MOSS LANDING MARINE LABORATORIES

SAN JOSÉ STATE UNIVERSITY

December 2016

Erika McPhee-Shaw, Ph.D.	Moss Landing Marine Laboratories
Olivia Cheriton, Ph.D.	United States Geological Survey
Mike Graham, Ph.D.	Moss Landing Marine Laboratories
Ivano Aiello, Ph.D.	Moss Landing Marine Laboratories

ABSTRACT

ENVIRONMENTAL DRIVERS OF BENTHIC-INTERIOR EXCHANGE EVENTS OVER THE CONTINENTAL SHELF OF MONTEREY BAY, CALIFORNIA

by Ben Yair Raanan

This study presents a comprehensive analysis of oceanographic data collected by an automated profiling mooring and fixed instrumentation platforms deployed over the mud belt on the southern continental shelf of Monterey Bay, California at 70 m depth during the fall of 2012. Physical and optical measurements taken at the study site documented the frequent occurrence of suspended particulate matter (SPM) layers in the mid-water column, the majority of which were detached from the seafloor and overlaid clearer water. This study examines the temporal and spatial variations of these detached SPM layers using time series analysis and modeling methods, and investigates how hydrographic and climatic phenomena relate to their appearance. The results indicate that the forcing of detached SPM layers appears to include not only large enough surface waves for recent seafloor resuspension in the bottom boundary layer but also, and of equal importance, energetic internal tides. A probabilistic model based on co-occurrence of the two environmental processes predicted the appearance of detached SPM layers with 77% accuracy. The ability of energetic internal tides to propagate into Monterey Bay appears to be, to some extent, connected to wind-driven shifts in stratification over the shelf.

ACKNOWLEDGMENTS

I would like to thank my advisor, Dr. Erika McPhee-Shaw, for her guidance and support throughout my time at Moss Landing Marine Laboratories. I am grateful for the advice I received from others working on this project, particularly Olivia M. Cheriton and Jeff Sevadjian and for the guidance of Tomoharu Eguchi. I would like to thank the crew of the R/V Point Sur all of the people who contributed to the October 2014 cruise.

This research was made possible by funds from the National Science Foundation, project OCE-0961810.

TABLE OF CONTENTS

LIST OF TABELS

LIST OF FIGURES

Introduction

Over continental shelves, particularly those of eastern boundary upwelling coasts, benthic-interior exchange (the supply of benthic material to the mid and upper water column) is important for ecosystem functioning and biogeochemical processes. Vertical distribution of suspended particulate matter (SPM) plays an important role in delivering benthic iron (a limiting micronutrient) and, potentially, benthic resting cysts of harmful algal species to the euphotic zone (Bruland et al., 2001; Ryan et al., 2005). Oceanographic surveys and the deployment of oceanographic systems off central California provide insight to the processes controlling suspension and redistribution of particulate matter on continental shelves. Local redistribution dynamics of suspended sediment transported within bottom boundary layer (BBL) flows have been well characterized in past studies by using fixed benthic instrumentation platforms and shipboard casts. However, mostly due to technological limitations, past observations were unable to adequately resolve SPM patterns carried in mid-water column (i.e., not at the seafloor) over the continental shelf due to temporal or event-scale variability of benthic-interior exchange processes. As such, our understanding of processes driving the transport of energy and matter to the mid-water column over continental shelves still remains incomplete, and so the ability to predict SPM mobility is limited. The work I present here employs innovative measurement platforms that collected high-resolution water column measurements over two month-long field deployments (fall 2011 and fall 2012). These observations were then processed to characterize events of exchange

between bottom boundary mixed fluid and the mid-water column over the continental shelf.

This study was part of a larger multi-institutional research project funded by the National Science Foundation (grant OCE-0961810 to lead PI McPhee-Shaw) to examine the exchange of SPM between the BBL and the water column interior over Monterey Bay's continental shelf. The project focused specifically on detached SPM layers (BBL intrusions of SPM rich water), often seen in the form of intermediate nepheloid layers (INLs) detaching from the continental margin. The research project entailed two month-long field deployments (fall 2011 and fall 2012) of an automated wave-driven profiling mooring and fixed instrumentation. Examining the fall 2011 observation period, Cheriton et al. (2014) document the frequent occurrence of layers of elevated SPM detached from the seafloor and provide evidence supporting a number of physical mechanisms (mainly associated with semidiurnal baroclinic internal tides of M_2 frequency) driving the intrusion and lateral advection of SPM layers. They suggest that rather than depending on a sole mechanism of injection, the formation of boundary intrusions may depend on a hierarchy of processes that occur over a range of time scales and combine to form favorable conditions for detachment and dispersal of well-mixed fluid and benthic constituents from the BBL into the interior water column. The multiplicity of contributing factors makes it difficult to clearly identify the underlying physical mechanisms responsible for boundary layer detachment and increases the complexity of identifying processes associated with benthic-interior exchange. Our comprehensive examination of the fall 2012 observations presented here serves as a base for comparison

and an extension of the 2011 dataset, by expanding the investigation of relationships between boundary intrusions of SPM and co-occurring environmental processes suggested by Cheriton et al. (2014).

Background

Sediment Resuspension and Transport Processes Near the Seabed

Sediment deposition on continental shelves results from a complex interplay of geological and oceanographic processes (Edwards, 2002). During major flooding events, fluvial sediment typically bypasses the littoral zone and is deposited offshore, either on or off the shelf (Eittreim et al., 2002; Syvitski & Morehead, 1999). For those sediments deposited on the shelf, subsequent transport is the result of both advective and diffusive processes. Sediment transport occurs during periods when bed shear stress is sufficient for erosion and transport (Nittrouer & Wright, 1994). On continental shelves, flux divergence in the sediment transport field (i.e., net erosion or deposition) can result from spatial gradients in wave energy, current velocity, or sediment properties (Harris & Wiberg, 2001).

Episodic, long-period energetic surface swell events play an important role in sediment erosion on continental shelves (Sternberg & Larsen, 1975). Over Monterey Bay's shelf and similar regions surface wave-induced bed shear stress has been identified as the primary driver for the resuspension of fine-grained silts and clays (George & Hill, 2008; Storlazzi et al., 2007). Enhanced near-bottom currents may also drive resuspension and transport of fine particulates over the shelf break and at some regions of the continental shelf. In many studies, such energetic bottom currents were observed as

sheared cross-shore current pulses that are thought to form as internal tides move shoreward and shoal into non-linear internal boars (NLIBs) (Boguckiet al., 1997; Bourgault et al., 2014; Cacchione & Southard, 1974; Carter et al., 2005; Dickson & McCave, 1986; Hosegood et al., 2004; Noble & Xu, 2003).

Upon resuspension, sediment particles are typically transported upward by turbulent eddies and vertical motions from the orbital velocities created by surface waves (Grant & Madsen, 1979). While the near-bottom forces associated with these waves may be sufficient to mobilize sediment within the wave-induced BBL, further destabilization and subsequent turbulence are required to efficiently propel sediment out of the BBL and further up into the water column. Observational studies (Carter et al., 2005; Cheriton et al., 2014; Hosegood et al., 2004; Jody M. Klymak & Moum, 2003), as well as laboratory and numerical modeling experiments (Aghsaee et al., 2012; Boegman et al., 2005; McPhee-Shaw, 2002), have suggested that enhanced vertical velocities generated during NLIW shoaling and breaking may not only bring sediment into suspension but also, in some cases, cause substantial vertical advection into or beyond the upper reaches of the BBL.

Advection of Sediment Beyond the BBL

Along the U.S. West Coast continental shelf, and particularly over Monterey Bay's mid-shelf, occurrences of boundary layer intrusions (layers of SPM detaching from the BBL) and detached SPM layers overlying clearer water are well documented (Carter et al., 2005; Cheriton et al., 2014; Klymak & Moum, 2003; McPhee-Shaw et al., 2004; Pak et al., 1980). There are several possible explanations for why SPM layers are often

found above the BBL over the continental shelf. For example, Cheriton et al., (2014) present evidence of strong, locally generated, vertical updraft events induced by the passing of large-amplitude internal waves of depression followed by an abrupt upwards isopycnal adjustment. The upward vertical velocities associated with these updrafts were shown to be sufficient for lifting particulates into the mid-water column from the BBL. Subsequently, this SPM may be focused by sheared lateral advection to form SPM layers overlying clearer water. Another hypothesized mechanism for detachment suggests that turbulent boluses or internal bores that are produced during the shoaling of internal wavetrains (Helfrich, 1992; Hosegood et al., 2004; Venayagamoorthy & Fringer, 2007) are capable of suspending and transporting particulates further up the slope, as the boluses decay, large particles may be redeposited to the bed and an intrusion of mixed fluid charged with fine sediment may disperse laterally along isopycnals offshore (Bourgault et al., 2014; Cheriton, McPhee-Shaw, et al., 2014; Hosegood et al., 2004).

Detached SPM layers in the form of intermediate nepheloid layers (INLs) have been observed over continental margins worldwide and are important for the transfer of energy and material such as sediment (Weering et al., 2001), nutrients (Nédélec et al., 2007), and organic material (Inthorn et al., 2006) from the shelf to the open-ocean and deep-sea environments. INLs can be defined generally as plumes or clouds of SPM independent from the surface mixed layer and either independent from or detaching from the BBL. Although the formation of shelf-depth INLs and detached SPM layers may be driven by several different mechanisms, the formation of deeper INLs detaching from the outer shelf and continental slope are most commonly attributed to critical reflection of the

internal tide (Azetsu-Scott et al., 1995; Cacchione & Drake, 1986; De Madron, 1994; Dickson & McCave, 1986; Gardner, 1989; Klymak et al., 2007; McPhee-Shaw et al,, 2004; Puig et al., 2004; Thorpe & White, 1988; Weering et al., 2001). Critical reflection occurs when the topographic angle of the slope matches the angle of internal wave phase propagation (normal to energy propagation; for a comprehensive review of this topic see McPhee-Shaw, 2006).

Processes Associated with Vertical Advection of Sediment

Cheriton et al. (2014) observed detached SPM layers over Monterey Bay's mid-shelf that exhibited a great deal of temporal variability and occurred under a variety of conditions. While some detached (or detaching) SPM layers appeared as stand-alone events, others appeared as a series of sequential events separated by mere hours. These detached SPM layers were frequently observed when winds were upwelling favorable, cold, dense bottom waters were present, and wave heights were >2 m. In addition, the presence of these detached SPM layers was strongly linked with energetic semidiurnal internal tides (Cheriton et al., 2014). Although the timing of strong internal tide forcing cannot be predicted (Nash et al., 2012), during the 2011 period of observation the influx of dense water up onto the shelf provided the sharp near-bottom stratification gradient, which supports the propagation of energetic internal tides into Monterey Bay (Cheriton et al., 2014b). This temporal variability and the wide range of co-occurring environmental conditions accompanying the appearance of detached SPM layers over the continental shelf of Monterey Bay suggest that these phenomena may be driven by more than one particular injecting mechanism, and that multiple processes, possibly fluctuating in

different time scales, combine to form favorable conditions for formation and transport of detached SPM layers (Cheriton et al., 2014).

Though the contribution of low-frequency oscillations in physical processes such as winds, internal tidal waves and high surface wave events to detachment of SPM layers still remains unclear, some of their effects are documented. For instance, despite the indirect relationship found by Cheriton et al. (2014) between resuspension of sediment by surface wave action and the timing of detached SPM features, availability of SPM in the BBL forced by high swell events is thought to be a first-order requisite for supplying seafloor material to the mid-water column (Cheriton et al., 2014). Additionally, wind-driven variations in bulk hydrographic shelf conditions (i.e., upwelling-relaxation dynamics) control stratification, which supports the propagation of internal tidal boars and other nonlinear internal waves thought to be important for the injection and transport of SPM. But to what extent do these processes influence the distribution and frequency of detached SPM layers? Do some processes increase (or decrease) the likelihood of observing detached SPM layers? If so, can that contribution be quantified? And finally, can we predict the presence of detached SPM layers based on these larger scale events? While the answers to these questions hold their own value, they may also advance our understanding of specific physical mechanisms that force the initial injection and subsequent distribution of detached SPM layers.

So far sufficient observational, laboratory and numerical modeling evidence has been gathered to suggest a number of mechanistic hypotheses for the formation of detached SPM layers over the mid-shelf. However, the stochastic nature of internal-wave

activity (Nash et al., 2012) accompanied by the mélange of changing hydrographic conditions typical to mid-shelf environments have prevented attaining a robust analytic and statistical description, let alone predictive framework, of these processes leading to the formation of detached SPM layers. The fall of 2012 dataset presented here, was used to examine the contribution of semidiurnal to weekly fluctuations in hydrographic conditions to the appearance of detached SPM layer. To attain a better quantitative description of the relationships between physical drivers and detached SPM layers, I incorporate a probabilistic approach to my work here in addition to other conventional correlation tests.

Research Objectives and Specific Questions

Objectives

Presented in this thesis are long-term, high-resolution observations of SPM over the southern Monterey Bay shelf gathered throughout the fall 2012 field effort of the NSF Benthic Exchange Project. The goals of this thesis research project are to (1) illustrate the temporal and spatial variation of detached SPM layers, (2) develop and implement time series analysis and modeling methods to investigate how hydrographic and climatic phenomena influence the appearance of detached SPM layers and manipulate erosional forces applied to the seabed, and finally, (3) to establish a predictive framework for appearance of detached SPM layers based on co-occurring environmental processes.

Specific Questions

1. What were the patterns of SPM over the mid-shelf of Monterey Bay during the period of observation (Fall, 2012)?

2. How did detached SPM layers vary in space and time and what were their transport pathways?
3. What were the principal sets of oceanographic conditions leading to the appearance of detached SPM layers?
4. How do changes in oceanographic conditions affect the likelihood of SPM features occurring at the study site? Can a probabilistic predictive model for the appearance of detached SPM layers be established based on co-occurring environmental processes?

Study Site

Located on the central California coast, Monterey Bay is a large, open embayment bisected by the Monterey Submarine Canyon, which runs east to west through the middle of the Bay (Figure 1). Local hydrography is strongly controlled by offshore winds (Breaker & Broenkow, 1994). The predominant northwesterly winds are strongest after the spring transition and drive the upwelling of cold, nutrient-rich waters from depths as deep as 300 m (Rosenfeld et al., 1994). The relaxation or reversal of this wind pattern allows warm surface waters to move back in over the shelf.

Energetic semidiurnal internal tides are known to be ubiquitous features of the shelves of Monterey Bay and the California coast. Internal tides in the wider Central California region are often dominated by the semidiurnal M2 constituent (Petruncio, 1993) but diurnal baroclinic motions dominate at some times and locations (Woodson et al., 2011). The intensity of internal tidal motions is controlled, in part, by the degree of stratification (Petruncio, Rosenfeld, & Paduan, 1998; Wang et al., 2009). Offshore in deep waters, energetic low-mode internal tides are generated at the nearby Sur Ridge

(Jachec et al., 2006) and propagate along the continental margin and into Monterey Canyon. Additional generation, as well as reflection and refraction, may occur both within the canyon and over the Monterey Bay shelf. The internal wave field over the shelf can include both onshore and offshore propagation (Carter et al., 2005; Cazenave et al., 2011) and is characterized by long-wavelength, low-mode semidiurnal waves, as well as high-frequency oscillations characteristic of nonlinear internal bores (Cazenave et al., 2011; Key, 1999; Stanton & Ostrovsky, 1998; Storlazzi et al., 2003; Walter et al., 2012; Woodson et al., 2011).

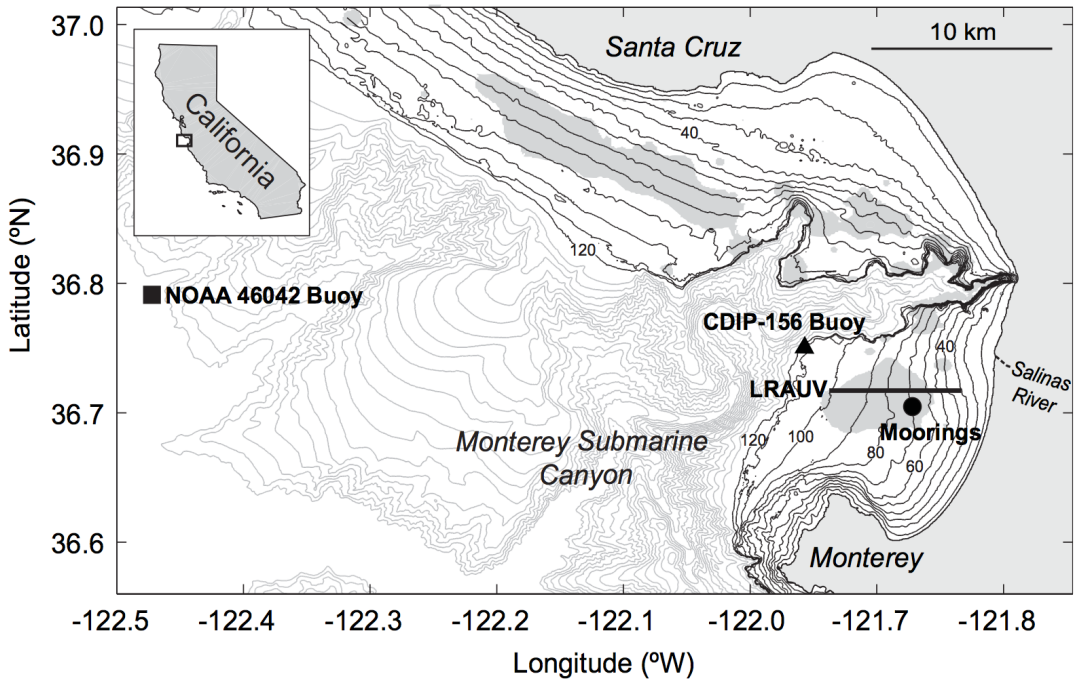

Figure 1. Map of 2011 and 2012 study site in southern Monterey Bay (Cheriton et al., 2014). Black dot is the site where the mooring instrument platforms (autonomous profiler, acoustic Doppler current profiler, and thermistor chain) were deployed. Locations of the NOAA 46042 (square) and CDIP-156 (triangle) buoys are also shown. Bathymetric contours are in 10-m from 0 to 100 m (black contours), and 100-m from 100 m to 2000 m (gray contours). The inset map shows the location of Monterey Bay along the coast of California, USA.

Over the Monterey Bay continental shelf and running northward, sits a band of fine-grained (diameter < 63 µm) sediment, predominantly made up of silt and clay-sized particles (Figure 1). The Salinas River (Figure 2) has been identified as the source of the mud-belt sediment on the southern Monterey Bay shelf (Edwards, 2002). Despite likely seasonal variations in resuspension, gridded grain size data derived from a series of sediment samples (n=43; Figure 2; usSEABED, 2006) show a seemingly consistent quasi-circular patch of mud on the southern Monterey Bay shelf (Edwards, 2002). This patch appears to be approximately 10-15 km in diameter, centered on the 70-90 m isobaths.

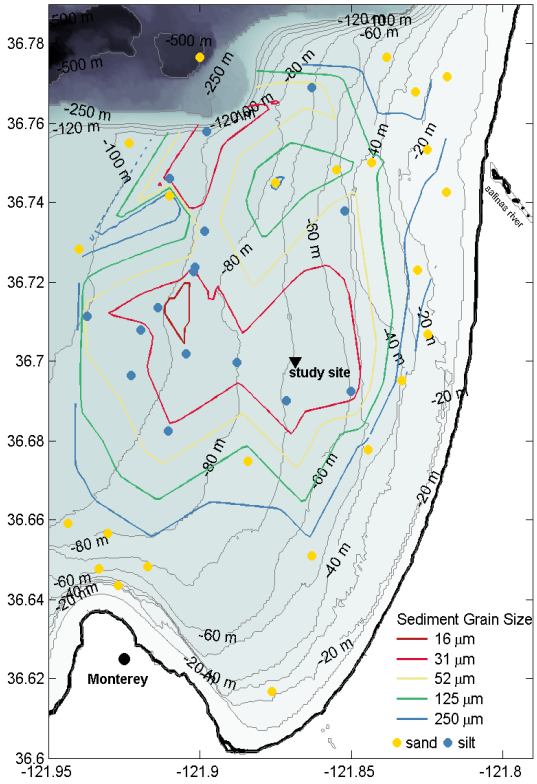

Figure 2. Sediment grain size distribution girded data superimposed over Monterey Bay's bathymetry. Blue (grain size<62µm, n=25) and yellow (grain size>=62µm, n=18) markers show the usSEABED (2006) sediment sampling points used for girding (n=43).

Methods

Field Experiment

From October 2 to October 28, 2012, a suite of instrumentation platforms (Figure 3) were deployed within 700 m of each other on approximately the 70 m isobath located on the mid-shelf mud belt of the southern Monterey Bay shelf (Figure 1). This field effort was designed to duplicate and extend the field deployment of September 24 to October 27, 2011 described by Cheriton et al (2014).

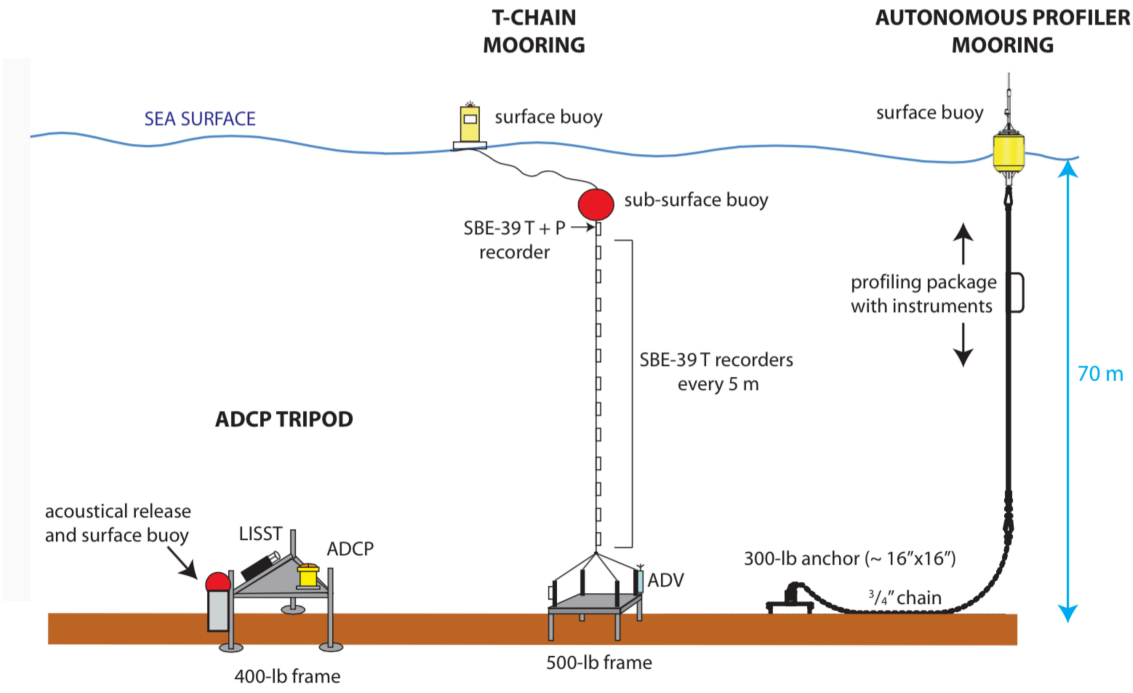

Figure 3. Diagram of moorings and instrumentation platforms with locations of ADCP, ADV, profiler, and thermistor chain.

Measurements of currents, temperature, and pressure. The instrumentation platforms included a thermistor chain mooring and a tripod with an upwards-looking Teledyne RD Instruments 300-kHz WorkHorse Sentinel acoustic Doppler current profiler

(ADCP; 36.7000°N, 121.8733°W). The ADCP collected current profiles with 2-m vertical bins every minute, with 25 pings per ensemble, resulting in an estimated uncertainty of ± 1.5 cm s^{-1}. The thermistor chain had 14 SeaBird SBE-39 thermistors sampling every 30 s; they were spaced 5 m apart from 1.5 to 61.5 meters above bottom (mab). The SBE-39 loggers at 1.5, 31.5, and 61.5 mab also measured pressure. Additional current and pressure measurements were sampled by a frame mounted Nortek Vector acoustic Doppler velocimeter (ADV) at 1.6 mab. Horizontal currents at the ADCP were rotated counter-clockwise 6.5^{o} according to local bathymetry to obtain along-shore (positive, northward) and cross-shore (positive, onshore) components.

Profiler measurements. An autonomous Brooke Ocean SeaHorse vertical profiler (on loan from Dr. Margaret McManus, University of Hawaii) outfitted with a SeaBird SBE-19plus CTD, SBE-43 oxygen sensor, WetLabs C-Star transmissometer, and WetLabs Wetstar chlorophyll-a fluorometer (Figure 4), was also deployed at the 70m isobath (36.7001°N, 121.8685°W). The profiler is wave-powered and uses a ratchet system controlled by an onboard microprocessor to move through the water column. Profiles between 9 mab and 1.5 m below the surface were undertaken each hour throughout the 1-month deployment period, resulting in a total of 667 profiles. Fifteen of these profiles were incomplete since the package did not reach the bottom of the mooring line upon descent. During the up-casts, the CTD on the profiler collected measurements at 4 Hz, for a vertical resolution of approximately 0.15 m. The profiler measured temperature, salinity, pressure, chlorophyll-a fluorescence, and beam transmittance. The resting position for the profiler was at the bottom of the cable, 9 m above bottom (at 60 m

depth). For further details on the operation of the autonomous profiler, see Cheriton et al. (2014) and Sevadjian et al., (2015).

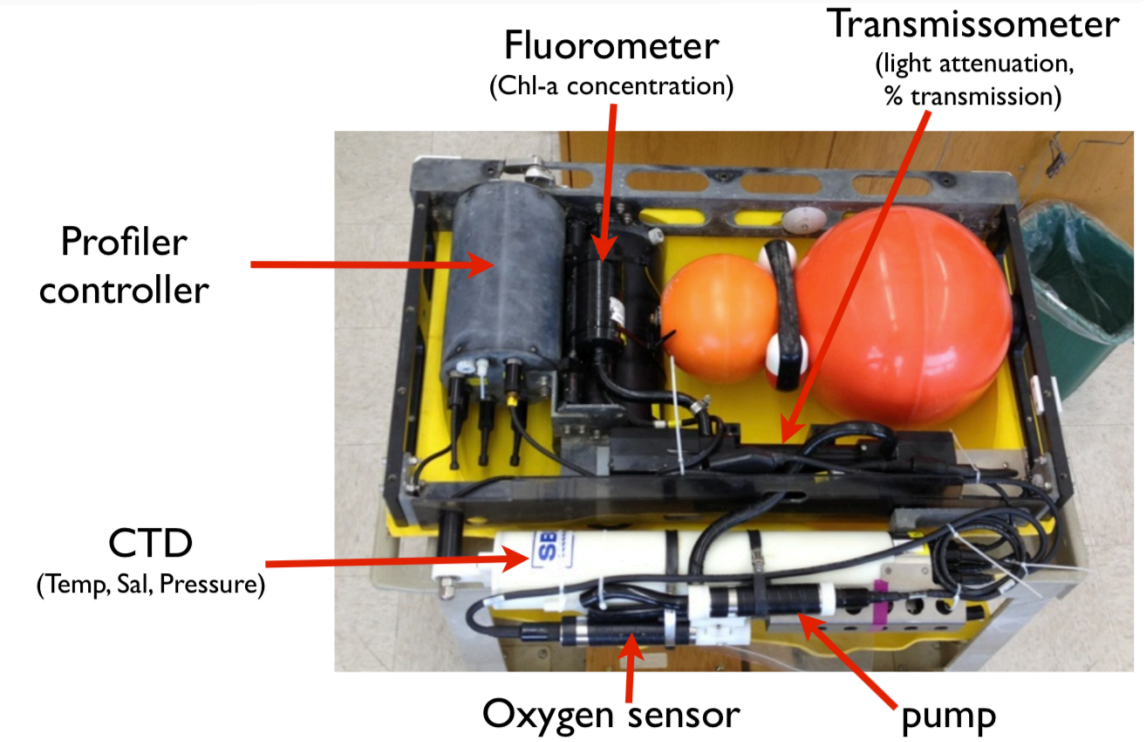

Figure 4. Brooke Ocean SeaHorse vertical profiler instrumentation. Photo by Olivia Cheriton, USGS. Used with permission.

Measurements of water turbidity. The autonomous profiler collected the primary dataset used in this study to detect detached SPM layers throughout the water column. The profiler instrumentation suite included a Wet Labs C-Star transmissometer, which measured beam transmittance (*tr*) at 650 nm over a 25 cm path length (*pl*). An identical device was attached to the ADCP frame at 0.4 mab to determine turbidity conditions in vicinity to the bed. Beam attenuation values (c, in m^{-1}) found to be linearly proportional to SPM concentrations were derived as $c = (-1/pl) * \log(tr)$ (McPhee-Shaw

et al., 2004). A linear fouling trend was present in beam attenuation dataset due to gradual accumulation of material on the transmissometer lens. To account for this, the trend calculated from a linear regression of the minimum values for each profile was removed from all beam attenuation data.

Wind, waves, tides, and river discharge. Hourly wind velocity data (Figure 8a) were obtained from the National Oceanic and Atmospheric Administration's (NOAA) Monterey buoy (Station 46042; www.ndbc.noaa.gov), located 27 nautical miles northwest of Monterey (36.785°N, 122.469°W; Figure 1). Tide levels and constituents were determined by applying a band-pass filter (10 h < period, T < 28 h) to pressure measurements from the ADV and using the t_tide software package (Pawlowicz et al., 2002). Surface wave parameters were taken from the Coastal Data Information Program (CDIP) Monterey Canyon Outer buoy (Buoy 156; cdip.ucsd.edu), located about 9 km offshore from the study site in 170 m of water (36.7608°N, 121.9469°W; Figure 1). The daily-averaged Salinas River discharge rates were obtained from the U.S. Geological Survey stream gauge located approximately 20 km inland from the coast (Site 11152500, http://waterdata.usgs.gov/nwis).

Data Processing

Data collected by the ODIM Brooke Ocean SeaHorse autonomous profiler were gridded to 0.1-m depth intervals to facilitate processing and analysis. Beam attenuation values *c* that exceeded the median from a 30-hr window by 4 standard deviations, were removed and replaced by cubic interpolations (to account for erroneous data logging) along with data from the 15 profiles that did not cover the entire water column. Water

column stratification at the study site was evaluated from high-vertical-resolution density profiles using the squared buoyancy frequency (Brunt-Väisälä), $N^2 = -g/\rho_o\,(\Delta\rho/\Delta z)$, where g is gravitational acceleration, ρ_o is the mean water density over a vertical profile, and ρ is density at a given depth, z. Squared buoyancy frequency values were used to determine the localized, temporal variations of water column stratification. The inertial frequency, $f = 2\Omega sin(\varphi)$, which characterizes oscillation associated with Earth's rotation (Ω), was calculated to be $f = 8.71\times10^{-5}$ rad/s (or T=20.02 hours) at the study site's latitude (φ=36.71^{o}N). Throughout this thesis I use "high frequency" to describe processes occurring at frequencies > f. Finally, vertical isotherm displacement ξ was calculated based on isotherm height above the bottom.

Throughout this project I performed variance-preserving power spectral density (PSD) analysis using the fast Fourier transform (FFT). For time series of interest, the time-mean was removed and the series was linearly detrended. Next, the data were split into smaller segments, which were then zero padded to achieve the next power of two for the FFT and to increase frequency resolution. The choice of window length signified a compromise between the increased number of degrees of freedom (DOF) for each spectral estimate, decreased frequency resolution, and length of the original record. Each segment was multiplied by a Hamming window with 50% overlap to decrease spectral leakage. Spectral densities were computed using the FFT, and segments were block averaged. Confidence intervals (95%) were calculated using a chi-square variable analysis and the "equivalent" number of DOF (Thomson & Emery, 2014).

Near-Bed Wave Orbital Velocity and Shear Stress Model

I computed estimates near-bed shear stresses from ADV current velocities (1.56 mab) and CDIP buoy directional wave measurements using the Grant-Madsen model (Madsen, 1994). For each time iteration, the MATLAB model (obtained from USGS) independently calculated frictional bottom shear stress due to orbital velocities from surface waves

$$\tau_w = \frac{1}{2}\rho f_w (u_b)^2 \quad (1)$$

where ρ is water density, f_w is the wave friction factor (Nielsen, 1992), and u_b is near-bed wave orbital velocity. The model also accounted for bottom shear stress induced by horizontal near-bed currents

$$\tau_c = \rho C_d u^2 \quad (2)$$

where ρ is water density, C_d is drag coefficient, and u is the magnitude of current velocity, and computed combined estimates of the total bed-shear-stress τ_{wc} due to surface waves and currents. Maximum wave orbital velocity values, u_b, were evaluated using the parametric spectral method described by Wiberg & Sherwood, (2008). This utilizes standard wave parameters and the Donelan spectral formulation method (Donelan et al. , 1985) which helps account for times when the wave parameters are inconsistent with a simple, unimodal spectral form.

In October 2012, a surface sample of seafloor sediment taken in the vicinity of the study site was found to be composed of 99.8% fine-grained sediment with D_{50} and D_{25} of 34 and 14 μm, respectively (Beckman Coulter LS Particle Size Analyzer result sheet; Appendix A). Based on this sample, estimates of bed shear stress were produced for both D_{50} and D_{25} grain diameters. To satisfy the model's input requirement for inner hydraulic roughness of the bed, I used a value of z_o = 9 x 10^{-5} m, which was a model-tuned estimate used for the soft, muddy portion of the Palos Verdes shelf in southern California by Ferré et al., (2010). The critical shear stress threshold, τ_{cr}, for mobilizing noncohesive sediment was calculated using the formulation described by Soulsby, (1997) as follows:

$$\tau_{cr} = \rho(u_{*cr})^2 \quad (3)$$

where ρ is water density and the critical shear velocity u_{*cr} is

$$u_{*cr} = \sqrt{(s-1)gd}\ \sqrt{\psi_{cr}} \quad (4)$$

where s is the ratio of sediment and fluid densities $(s = \rho_s/\rho_f)$, g is gravitational acceleration, d is grain diameter and, ψ_{cr}, is the derived Shield parameter for initiation of sediment transport. This gave τ_{cr} = 0.08 N m^{-2} for the silt (D = 34 μm) sediment at the study site, which matches the critical value used by Dunbar & Barrett, (2005) and Cheriton et al., (2014) to determine the threshold for the resuspension of shelf muds.

I performed time-series analysis of the different model outputs (i.e., τ_w, τ_c and τ_{wc}) to evaluate whether detached SPM layers are associated with particular processes

such as erosion due to large surface waves or near-bottom currents. I also performed a spatial analysis of surface wave-induced bed shear stress (τ_w) spanning the entire southern bay shelf (20 to 100m isobaths) to illustrate how τ_w varied. I then passed the model outputs through lagged cross-covariance functions and probabilistic statistical classification models (described below) to characterize the relationship between observations of detached SPM layers and frictional bottom shear stress and to determine whether the occurrence of detached SPM layers was directly related to local sediment resuspension events.

Optical Peak Identification Algorithm

The temporal variability and vertical distribution of observed detached SPM layers (first and second questions driving this study) were determined by a MATLAB algorithm designed following methods by Cheriton et al., (2014), Sullivanet al., (2010) and Sevadjian et al., (2015). I designed the algorithm to identify detached optical peaks of SPM (i.e., elevated SPM overlying clearer water) in individual vertical profiles collected by the profiler by examining the fine-scale vertical structure of corrected beam attenuation values. The iterative algorithm first extracted and smoothed individual profiles using a digital low-pass filter and subtracted the background attenuation level, then, local maxima and minima were identified by analysis of first and second derivatives of the signal computed with respect to depth. The "level of intensity" of each optical peak was determined by computing a ratio (At_{ratio}) between the peak's maximum attenuation value (At_{max}) and the nearest local minima (At_{min}) located under it (i.e., $At_{ratio}=At_{min}/At_{max}$). detached SPM layer(s) were defined as $At_{ratio}<0.66$ (Figure 5). To

avoid false detection, I only considered peaks with At_{max} within the top 15th percentile of the beam attenuation record. I defined the upper and lower extents of the layer as the profile's intersection with half of the peak's maximum attenuation value (0.5*At_{max}; Figure 5). A second filtering criterion eliminated peaks found in the upper half of the water column. I used the products of the algorithm to index profiles that recorded detached SPM layers and serve as a base for further analyses throughout this project.

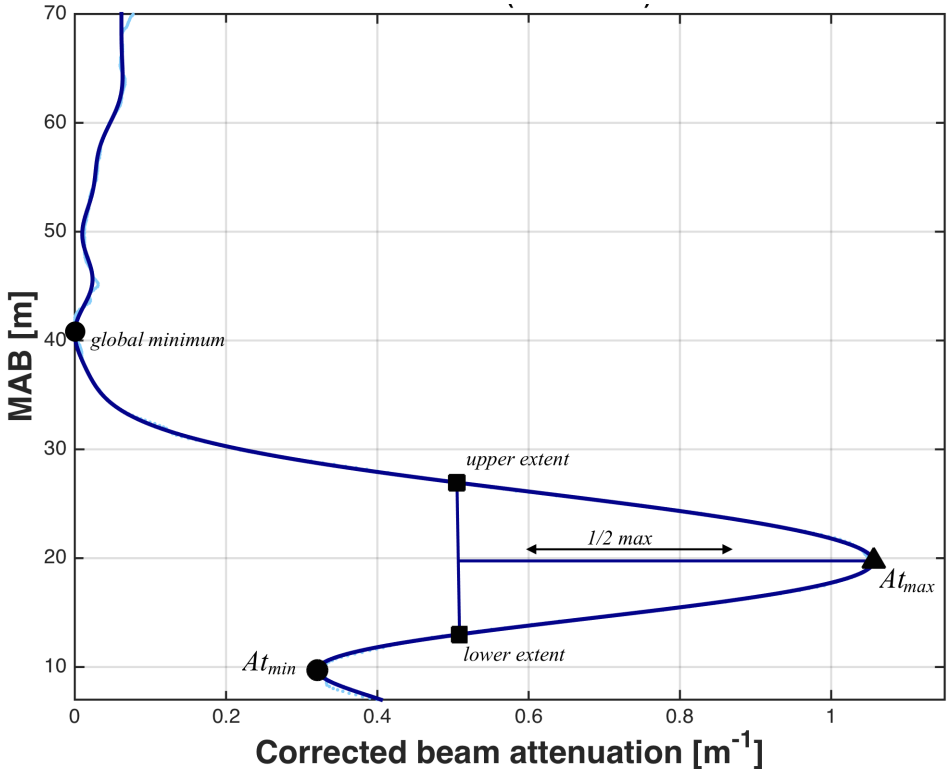

Figure 5. Example profile of a corrected beam attenuation (*c*) profile showing how SPM layer attributes were identified. The smoothed profile (dark blue line) is overlying the original profile (light blue dotted line), the triangle is the peak (At_{max}), the circles indicate upper (global) and local lower minima (At_{min}), and the squares mark the upper and lower extent of the layer ($1/2*At_{max}$).

Suspended Particle Trajectory Model

The shelf excursions of detached SPM layers were estimated using a simple 3-dimensional particle-trajectory model, designed following Cheriton et al.'s (2014)

particle tracking model concept. The model calculated particle displacement by using the ADCP-measured current velocity for the horizontal component, and, for the vertical component, the ADCP-measured vertical velocities with the estimated Stokes particle settling velocity (D=34 μm) of $w_s = 7\text{x}10^{-4}$ m s^{-1} subtracted. Particle settling velocity was calculated according to Stokes Law of settling (Stokes, 1851)

$$W_s = \left[g \frac{(\rho_s - \rho_f)}{18\mu} \right] D^2 \qquad (5)$$

where w_s is settling velocity, g is gravitational acceleration, ρ_s is sediment density, ρ_f is fluid density, μ is the dynamic viscosity of seawater, and D is the particle diameter.

To initialize the model, I used the temporal and vertical positions of the detached SPM peaks located by the optical peak identification algorithm as inputs. The model then assumed that a "particle" is present at this depth and time at the location of the profiler on the shelf (i.e., x = 0, and y = 0 at time of peak detection). The model tracked this particle forward in time from this initial point using progressive vectors, and stopped as soon as the particle reached the seafloor (or in some cases sea-surface). To investigate the possible origin and pathway the particle took before reaching the profiler site, the model also ran backwards in time, using reversed progressive vectors. Total model run time was 24 hours in each direction.

Studies show the importance of larger suspended particulates for sediment accumulation on continental shelves (Sternberg & Ogston, 1999) as fine suspended particles generally combine to form flocs and aggregates (125 to 750 μm), and thus considerably increase particle settling velocity (Eisma, 1993). To simulate flocculation,

the model replaced particle settling velocity with an empirically measured aggregate settling velocity of $w_s = 4x10^{-3}$ m s^{-1} which corresponds to a 250 μm diameter floc (Ogston & Sternberg, 1999). Aggregation was tested at different scenarios in which settling velocity replacement is simulated at different times past the initial particle measurement (time = 0). I used the outputs of this analysis to approximate transport pathways of the suspended matter entrained within the detached SPM layers and to provide means for addressing the second question driving this study.

Identifying Predictors of Detachment

Time-domain empirical orthogonal function (EOF) analysis. In many cases, gaining insight to the underlying processes driving vertical mixing can be challenging due secondary processes that introduce a considerable amount of variance ("noise") into the system. In order to assess the relative importance of the various processes contributing to the appearance of SPM layers, I decomposed observations of current velocities and turbidity using a time-domain empirical orthogonal function (EOF) analysis (Glover, Jenkins, & Doney, 2011; Thomson & Emery, 2014) and examined the vertical structure and the temporal patterns of the first two modes of variability. Lucas, Franks, & Dupont, (2011) showed that EOF decomposition was effective in extracting the internal-tide signal from other modes of variability in current velocity time series. Interpretation of the EOF modes was achieved by extracting the time series of the EOF amplitude and performing variance preserving PSD analysis.

Lag cross-correlation coefficient function. Unlike high-frequency physical parameters, such as vertical isotherm displacement (ξ), which have been shown to be

closely coupled to local turbulent dissipation and mixing events (Carter et al., 2005; Klymak et al., 2007; Woodson et al., 2011), lower-frequency forcers of mixing are expected to exhibit indirect (time-lagged) associations to observations of benthic-interior mixing events. I computed lagged cross-correlation coefficients (Equation 6 and Figure 6) along with 95% confidence intervals to identify the lag time scales associated with relationships between time series of interest. Following methods described by Thomson & Emery, (2014) and Glover, Jenkins, & Doney, (2011), the cross-correlation coefficient, r_n, of two time series (x and y with means of $\bar{x}$ and $\bar{y}$) at lag *n* with *N*-*n* pairs over lapping is given in its definition as:

$$r_n = \frac{N}{N-n-1} \frac{\sum (x_i - \bar{x}|_{n+1}^{N})(y_{i-n} - \bar{y}|_{1}^{N-n})}{\sqrt{\sum (x_i - \bar{x}|_{n+1}^{N})^2 (y_{i-n} - \bar{y}|_{1}^{N-n})^2}} \quad (6)$$

Probabilistic Predictive Framework

Logistic regression classification model. To further assess the relative importance of terms contributing to the appearance of detached SPM layers and to create a predictive model for the appearance of intrusions based on co-occurring environmental processes, I implemented logistic regression under the generalized linear model (GLM) framework described by Krusche, (2010) and Gelman & Hill, (2006). Logistic regression is the standard way to model binary outcomes, that is, data Y that take on the values 0 or 1 (i.e., detached SPM layer absence or appearance, respectively; Gelman & Hill, 2006).

As shown in Table 1 and in Figure 7, logistic regression is implemented to find the equation that best predicts the value of the Y variable for each value of the X variable.

What makes logistic regression different from linear regression is that the Y variable is not directly measured; it is instead the probability of obtaining a particular value of a nominal variable (i.e., 0 or 1; Figure 7). Additionally, in this case logistic regression is preferable over more commonly used null hypothesis significance testing (NHST) methods, as it allows us not only to see whether the probability of getting a particular outcome is associated with the measurement variable, but also to predict the probability of getting a particular outcome, given the measurement variable. Finally, logistic regression may be performed with a single metric predictor as well as an additive combination of multiple metric predictors. The outcomes of this analysis provide means for addressing the third and fourth questions driving this study.

Table 1

Equations used for computation of Logistic regression

Description	Equation	Variables
Logistic function (sigmoid function)	$sig(x) = \frac{1}{(1+e^{-x})}$	x = measurement variable
Logit function (inverse of the logistic function)	$logit(p) = ln\left(\frac{p}{(1-p)}\right)$	p = the probability that Y=1, for $0 < p < 1$
Logistic regression model (written in terms of the *logit* function)	$\ln\left(\frac{p(y=1)}{p(y=0)}\right) = \beta_0 + \beta_1 x_1 \ldots$	p = probability, x = measurement variable, $\beta_{0,1}$ = regression coefficients
Logistic regression model (written in terms of the *logistic* function)	$p(y=1) = \frac{e^{\beta_0+\beta_1 x}}{1+e^{\beta_0+\beta_1 x}}$	p = probability, x = measurement variable, $\beta_{0,1}$ = regression coefficients

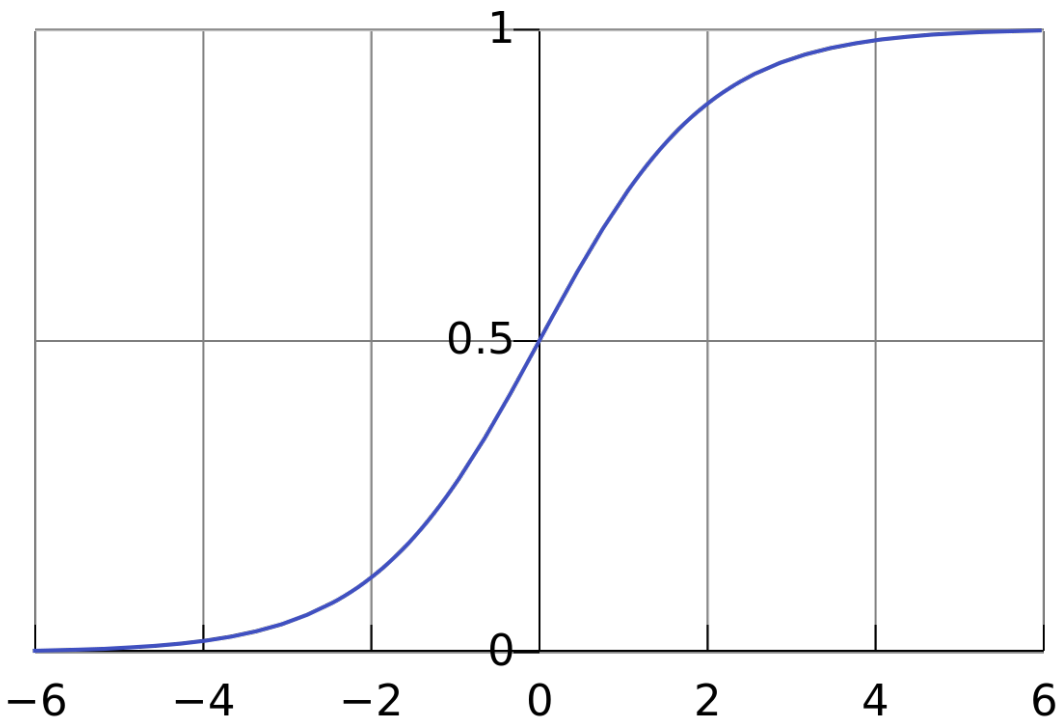

Figure 6. An example of the logistic sigmoid function of a single variable, with the measurement variable on the horizontal axis and the probability for the outcome of the dependent variable (between 0 to 1) on the vertical axis.

Receiver operating characteristic (ROC). To illustrate the performance of each binary classification model, I computed a receiver operating characteristic (ROC). ROC analysis provides a metric commonly used to evaluate the quality of binary classifiers and to select possibly optimal models over suboptimal ones. For each output of the binary classifier, I applied threshold values across the interval [0,1]. For each threshold, two values were calculated, the True Positive Ratio (TPR)

$$TPR = \frac{\sum True\ positive}{\sum True\ positive + \sum False\ negative} \quad (7)$$

and the False Positive Ratio (FPR).

$$FPR = \frac{\sum True\ negative}{\sum True\ negative + \sum False\ positive} \quad (8)$$

A ROC curve illustrating the classification performance of a model can then be constructed by plotting TPR and FPR against each other. The area under the curve (AUC) statistic is a commonly used metric for model comparison; a high AUC of 1.0 indicates perfect classification while random guessing normally yields a low AUC score of 0.5.

Results

Hydrographic and Meteorological Conditions

The full record of meteorological and hydrographic variables is given in Figure 8.

Wind-driven upwelling and water-column response. The principal component of winds at the offshore NDBC station 46042 was oriented at 336°, roughly parallel to the coast (i.e., upwelling favorable; Figure 8a). The 4-week study period was characterized by several periods of sustained upwelling-favorable winds (northeasterly), that were interrupted by weakening or full reversals to downwelling-favorable winds sometimes lasting up to a few days at a time.

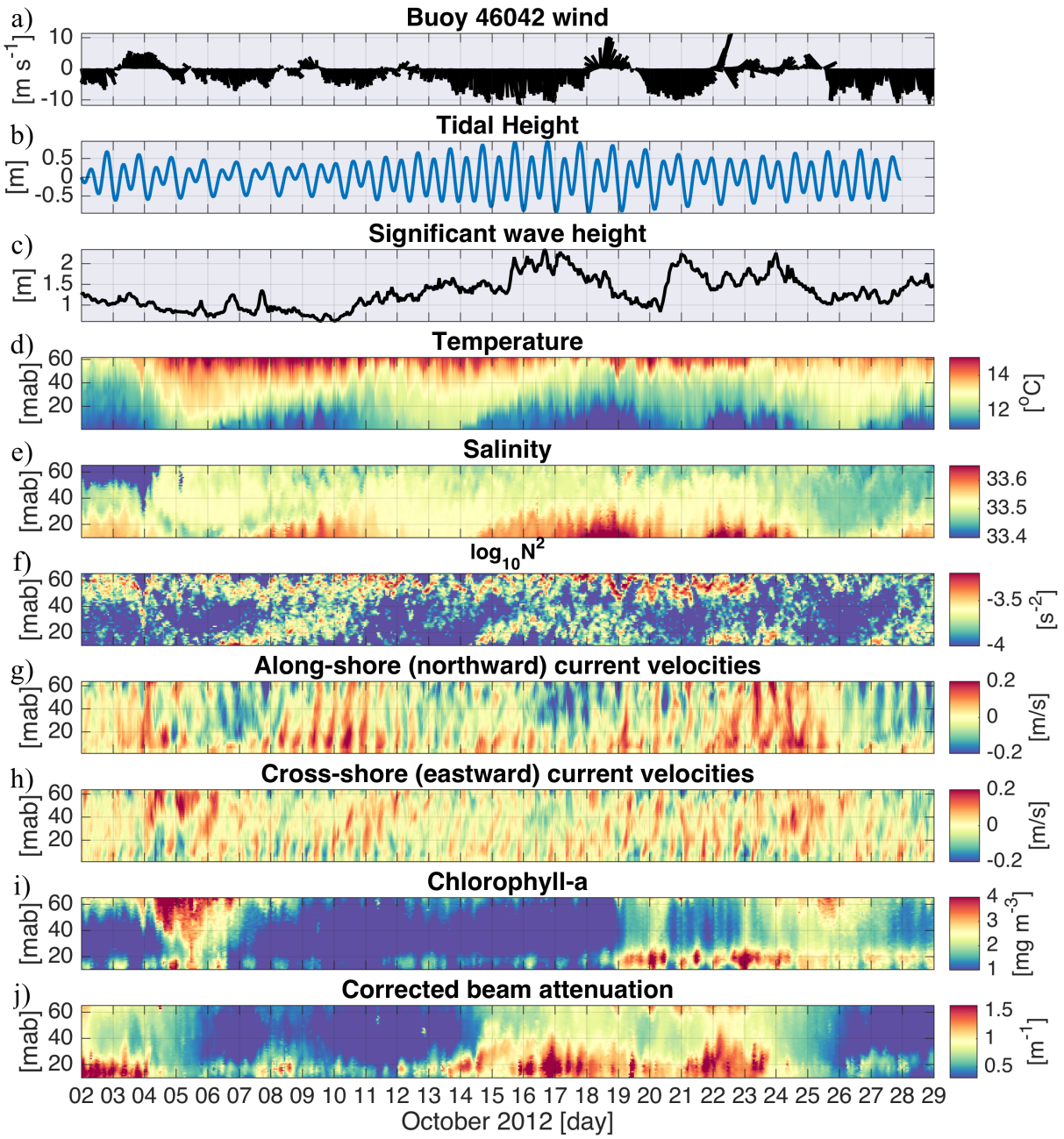

Figure 7. Time series data collected over study period, from 2 to 29 October 2012 (PST). (a) Wind velocity, (b) water level height above mean, and (c) significant wave height, as well as data from the profiler: (d) temperature, (e) salinity, (f) log10 of the squared Brunt–Väisälä frequency, N^2, (g) across-shore velocity, (h) along-shore velocity, (i) chlorophyll-a, and (j) corrected beam attenuation.

The month-long period captured 4 distinct upwelling periods, with start times of 5, 12, 19, and 25 October (Figure 9a). Within approximately 1.5 days after the start of upwelling-favorable winds, cold, dense water infiltrated the bottom portion of the water column over the shelf (Figure 9a, 9b). When the equatorward winds relaxed, or reversed, the flow within the bay shifted poleward and the water column rapidly warmed. These observations of lagged wind/water-column response are confirmed by lagged cross-covariance analysis of upwelling-favorable wind and 11.5°C isotherm displacement (Figure 10) and are in agreement with previous descriptions of the water-column response to upwelling dynamics over the Monterey Bay shelf (Cheriton et al., 2014; Storlazzi et al., 2003).

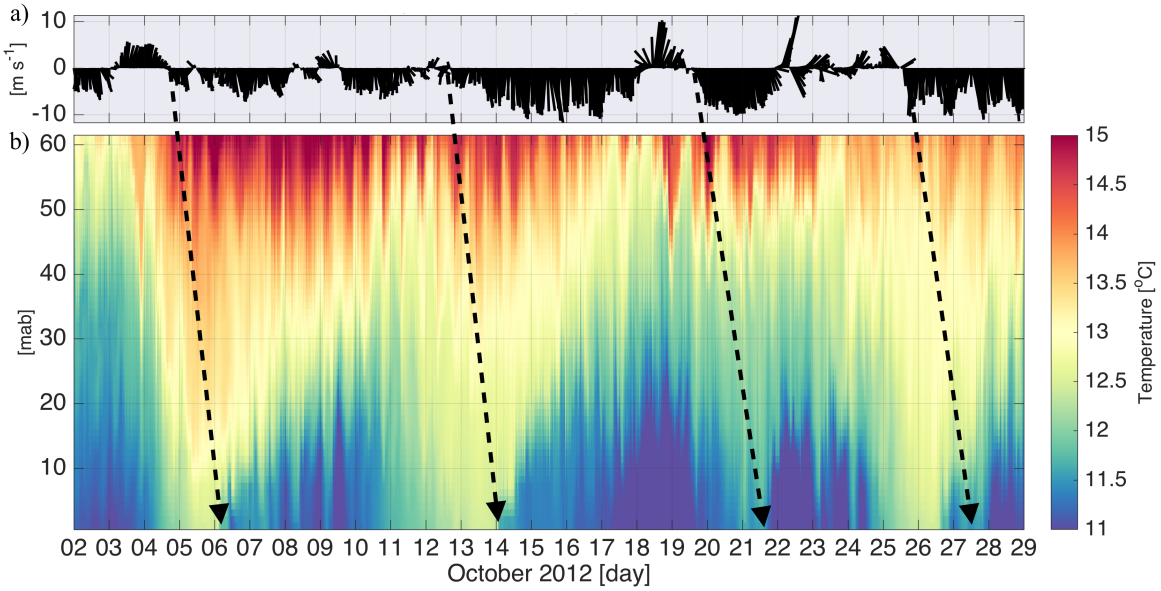

Figure 8. Lagged relationship (dashed arrows) between buoy 46042 uppwelling-faverable winds (a) and water column tempratures collected by thermistor chain. ~1.5 days after the start of upwelling-favorable winds cold water infiltrated the bottom portion of the water column. Wind reversals are followed by rapid warming.

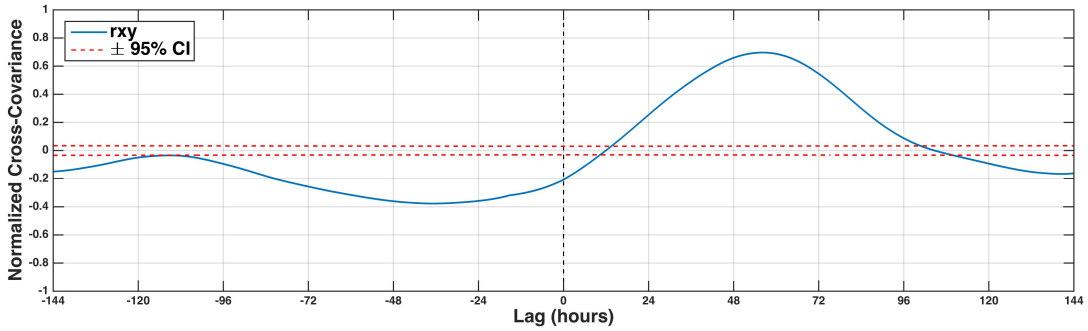

Figure 9. Lagged cross-covariance analysis of upwelling-favorable wind and isotherm displacement ξ11.5 show segnificant correlation beetween the above at lags of approxemtly 24-84 hours. The 95% confidance intervals are indicated by red dashed lines.

During the period of observation, cold upwelled water infiltrated onto the shelf and formed a secondary pycnocline, that gradually shoaled as the cold bottom Ekman layer reached further up into the water column (Figure 11a; approximate depth of the secondary pycnocline depth is indicated by the 12 °C isotherm). This near-bottom pycnocline was of similar strength ($N \sim 2 \times 10^{-2}$ s^{-1}) to the near-surface pycnocline and appeared on the shelf through multiple upwelling periods. The water below the secondary pycnocline was dense and unstratified.

Throughout the one-month deployment, and especially during the major upwelling event of October 14 to 25, the appearance of the secondary pycnocline during upwelling periods coincided with increased high-frequency displacement of near-bottom isotherms (Figure 11b). The high-frequency ($>f$) fluctuations in bottom temperatures were most energetic at the M_2 semidiurnal frequency (Figure 12) and can be thought of as the onset of upwelling seen as a series of internal tidal bores propagating near the seabed along secondary pycnocline. Identical observations were reported by (Cheriton et al., (2014b), which used the same dataset, as well as data collected further down the shelf, to

explore the control of regional Ekman dynamics on propagation of internal waves through continental shelf waters. Their results are similar to other studies conducted over the shelf of Oregon by (Klymak et al., 2007; Klymak & Moum, 2003), and demonstrate the importance of cross-margin, upwelling-driven, shelf hydrography to the formation of wave guides that allow the propagation of internal wave energy at both tidal and higher frequencies.

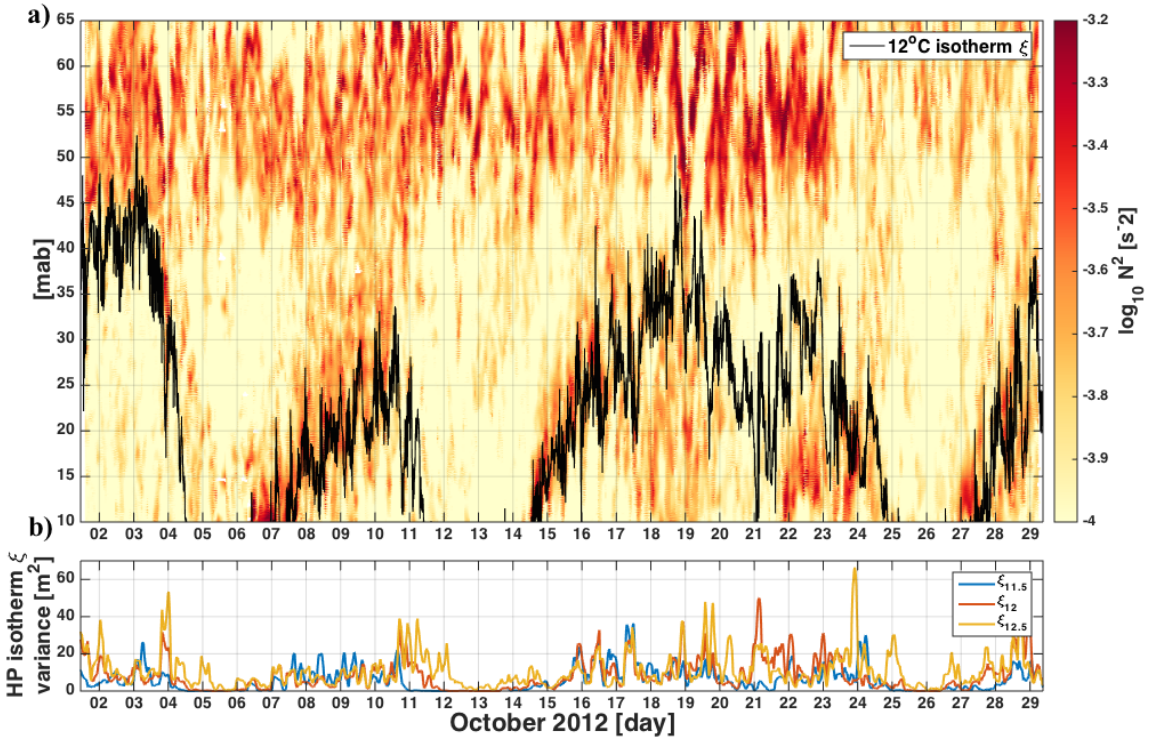

Figure 10. (a) Squared Brunt-Väisälä frequency, N2, in log10 scale, with the 12°C isotherm overlaid (black line), indicating the approximate depth of the near-bed, secondary pycnocline. Bottom panel (b) shows increased variance in high-passed (f) near-bottom isotherm displacement (ξ), an indicator for high-frequency (>*f*) fluctuations.

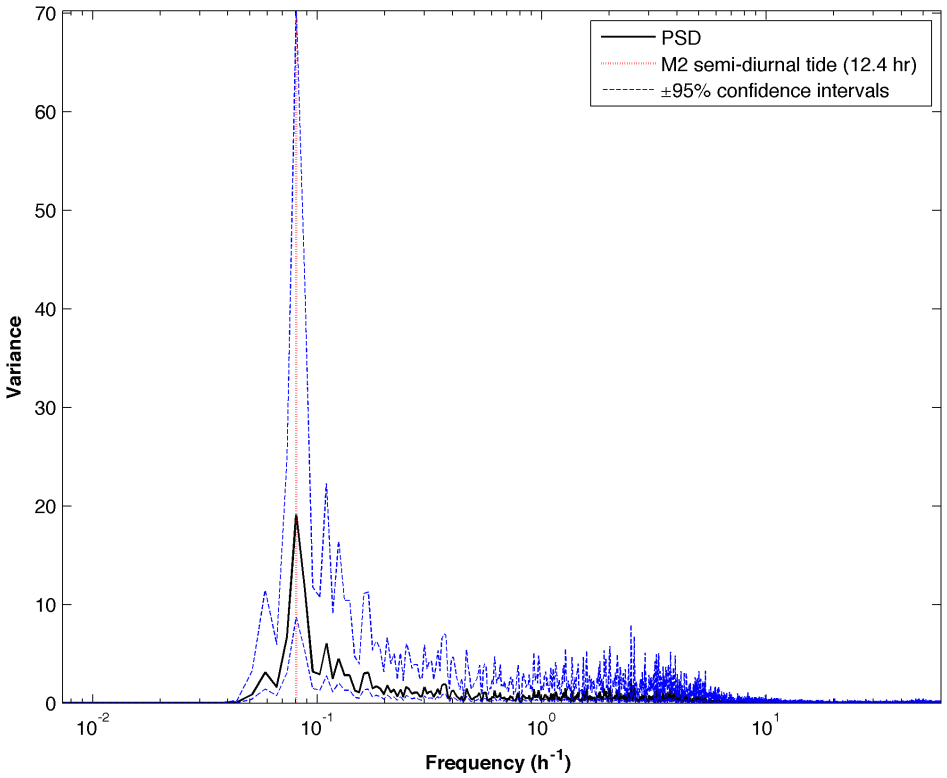

Figure 11. Variance-preserving power spectral density (PSD) of high-passed (>*f*) near-bottom isotherm displacement $\xi_{11.5}$, presented along with 95% confidence intervals. The variability is most energetic at the M_2 semidiurnal tidal frequency shown as vertical dashed red line.

Surface-waves. Significant wave height measured at the CDIP buoy during our study period had an overall average of ~1.3 m and co-varied with winds (Figure 13b), especially during the third and fourth upwelling periods, which coincided with several larger-than-average surface swell events measuring wave heights of over 2 m (15–18 October, 21 and 24 October; Figure 13a).

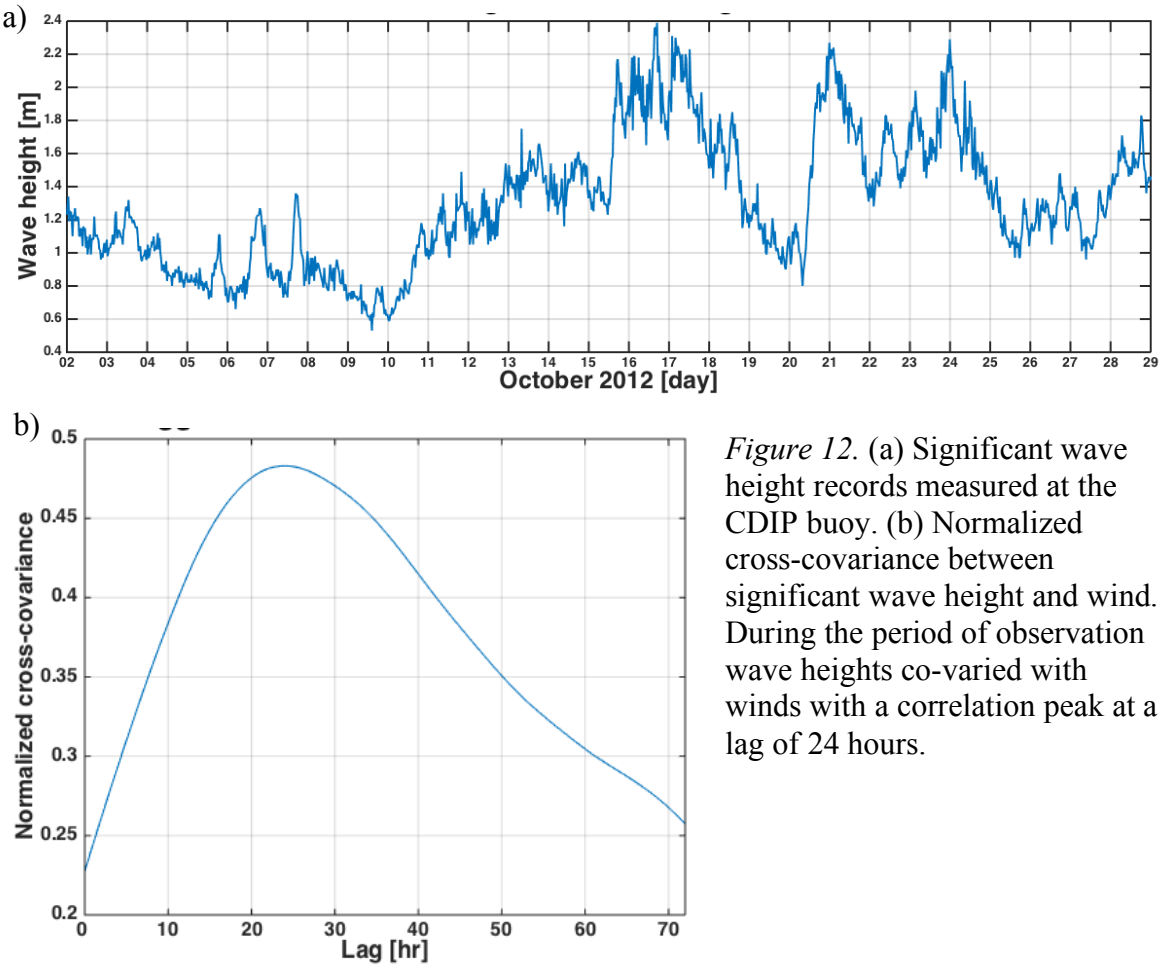

Figure 12. (a) Significant wave height records measured at the CDIP buoy. (b) Normalized cross-covariance between significant wave height and wind. During the period of observation wave heights co-varied with winds with a correlation peak at a lag of 24 hours.

Tidal height. T-tide harmonic analysis of tidal height measurements based on ADV and thermistor pressure had dominant semidiurnal (M_2 T=12.41 hr) and minor diurnal (K_1, T=23.93 hr and O_1, T=25.82 hr) signatures (Figure 14a, b). The max spring tide occurred on October 16-17, and neap heights were observed 7-8 October.

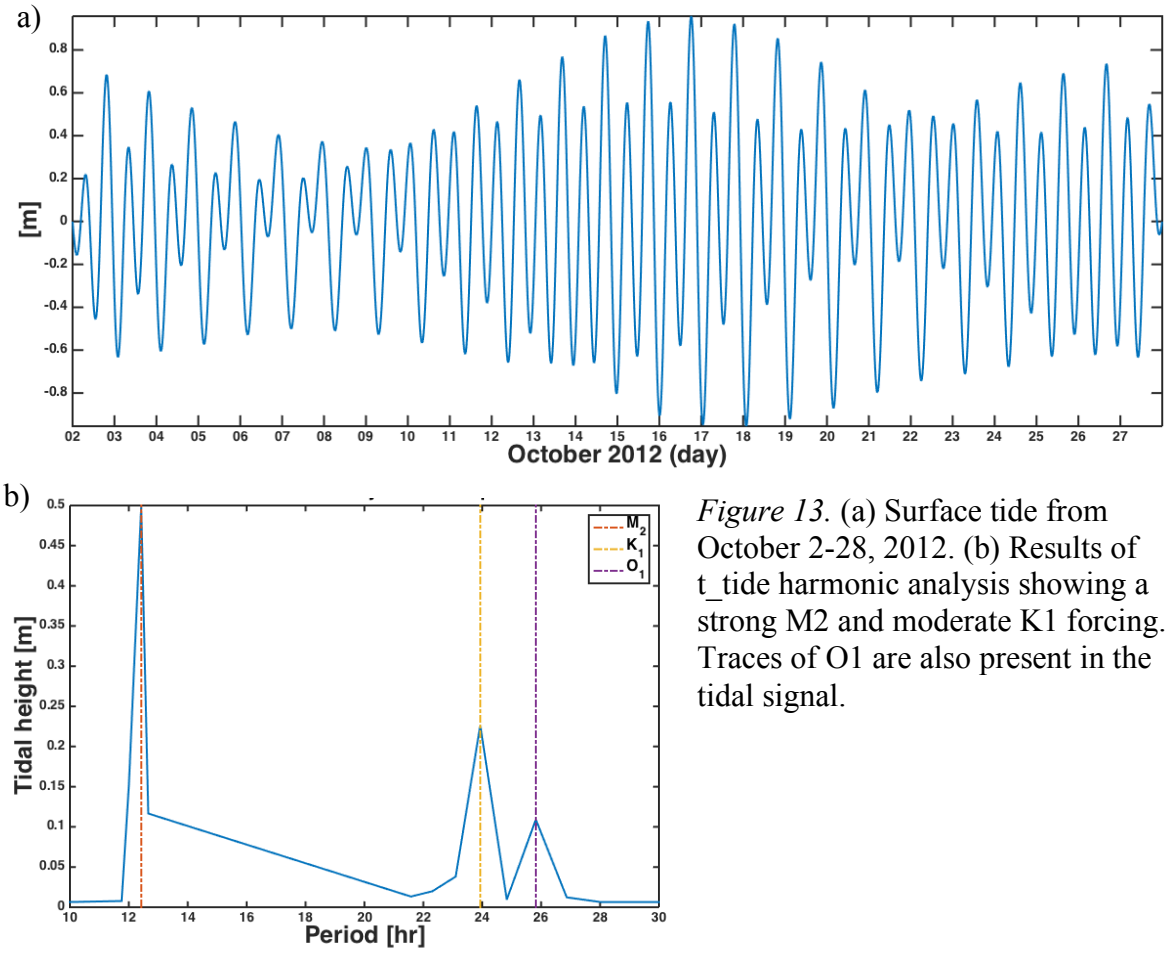

Figure 13. (a) Surface tide from October 2-28, 2012. (b) Results of t_tide harmonic analysis showing a strong M2 and moderate K1 forcing. Traces of O1 are also present in the tidal signal.

Salinas river discharge. The mean Salinas River discharge rate during our study period was ~0.9 $m^3 s^{-1}$, with the largest river discharges (>1.5 $m^3 s^{-1}$) occurring on 6 October and 16 October 2012. While these rates are higher than typical monthly averaged values for September and October (0.2 and 0.1 $m^3 s^{-1}$, respectively, for years 2000–2010), these rates are still low enough that it is unlikely the lagoon outflow was breached (historically, the sand dunes that block the river outflow are bulldozed by local municipalities only under winter flood conditions). For comparison, the mean discharge

for January–May 2012 was ~32.0 m^3 s^{-1}. Thus, the Salinas River (Figure 1) was not a major source of sediment to the bay during the study period.

Comparison to conditions during 2011 deployment. For comparison and reference, the hydrographic and meteorological conditions recorded during the 2011 field effort (September 24 to October 27) are shown in Figure 15.

The general hydrographic and meteorological trends observed during the 2011 deployment are very similar in pattern and magnitude to the prevailing conditions recorded during the 2012 study with two exceptions: First, the baseline of significant wave heights measured during the study period of 2011 (Figure 15c) was larger in magnitude and high swell events were more persistent than in the fall of 2012 (Figure 8c and Table 2). Second, during the 2011 deployment near-bottom water temperatures were almost 1^{o}C lower than in 2012 and bottom water masses had higher salinities (and densities) than observed the following year (Figure 15d, e). Interestingly, the magnitude and persistence of upwelling favorable winds were practically identical during the two periods, suggesting that the differences in water-column temperatures might have been driven by meso/synoptic scale variability, or alternatively, by more local near bottom mixing mechanisms. Summary of the differences is given in tables 2 and 3. For a more detailed description of fall 2011 conditions, refer to Cheriton et al., (2014).

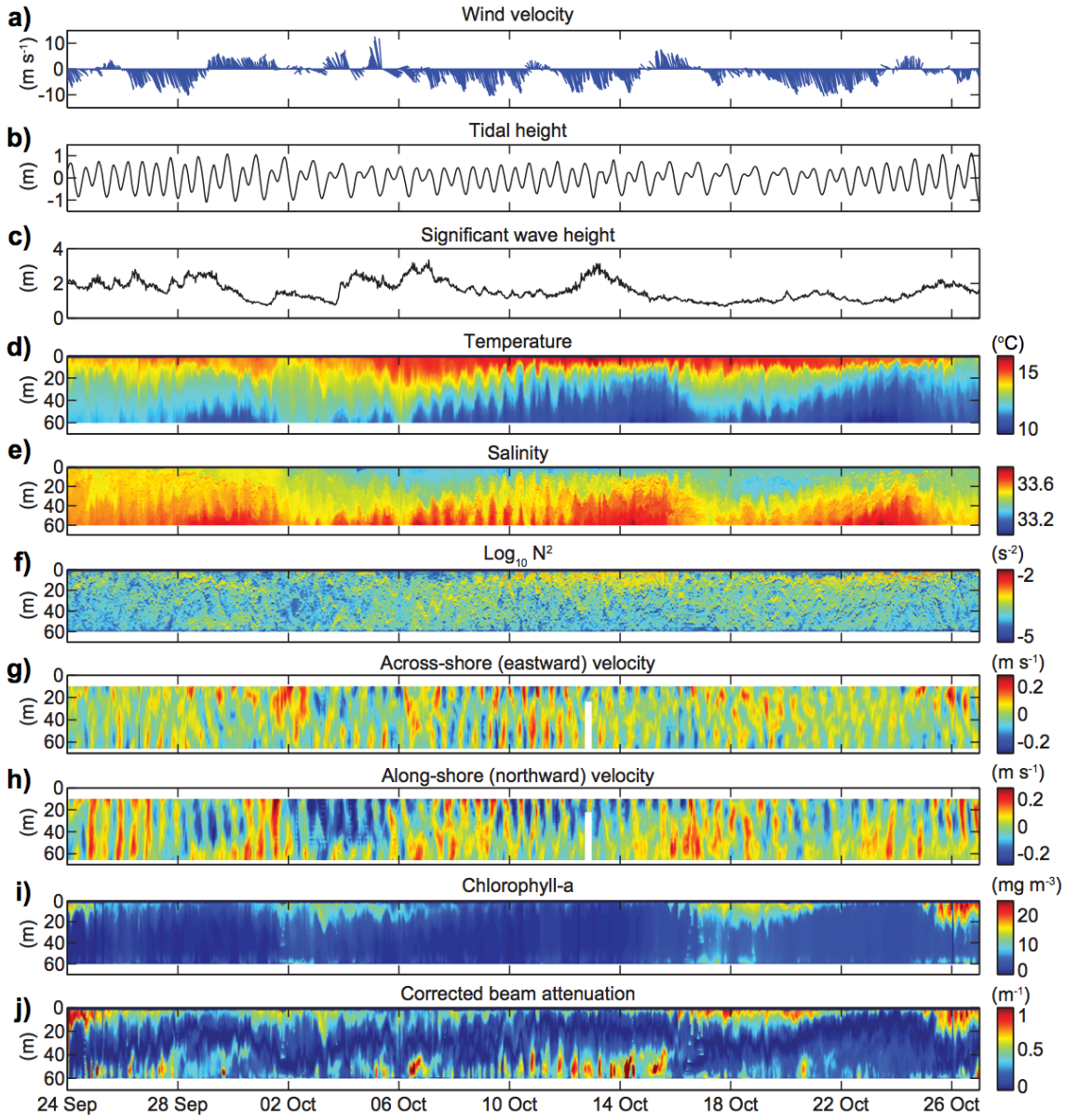

Figure 14. Time series data collected over study period, from 24 September to 27 October 2011 obtained from Cheriton et al. (2014). (a) Wind velocity, (b) water level height above mean, and (c) significant wave height, as well as data from the profiler: (d) temperature, (e) salinity, (f) log10 of the squared Brunt-Brunt–Väisälä frequency, N^2, (g) across-shore velocity, (h) along-shore velocity, (i) chlorophyll-a, and (j) corrected beam attenuation (c*).

Table 2

Fall 2011/2011 comparison of meteorological conditions

	Buoy 46042 upwelling favorable winds			CDIP 156 significant wave height		
	Mean ± SE[+] (m/s)	Max (m/s)	% of time upwelling	Mean ± SE[+] (m)	Max (m)	% of time >2m
2011	2.6 ± 0.12	12.05	72%	1.3 ± 0.02	3.3	22%
2012	3.5 ± 0.12	12.70	78%	1.5 ± 0.02	2.3	5%

[+]Standard error to the mean (α=0.05)

Table 3

Fall 2011/2011 comparison of water column temperatures and salinities

	Mean Temp (^{o}C)			Mean Salinity		
mab	2012	2011	ΔTemp[+]	2012	2011	ΔSal[+]
61.5	14.25	14.48	-0.22	33.46	33.41	0.058
51.5	13.45	13.22	0.22	33.48	33.44	0.041
41.5	12.88	12.46	0.42	33.50	33.48	0.013
31.5	12.51	11.88	0.63	33.51	33.53	-0.021
21.5	12.18	11.39	0.78	33.53	33.57	-0.042
11.5	11.75	10.91	0.83	33.56	33.61	-0.053
0.5	11.39	10.58	0.81	-	-	-

[+]*Δ* defined 2012-2011

EOF analysis of ADCP currents and energetic internal tides. Semidiurnal variability, dominated current velocity fields over the course of the field experiment (Figure 16). Semidiurnal cross-shore currents exceeded 0.25 m s^{-1} near the surface and bottom during energetic internal tides.

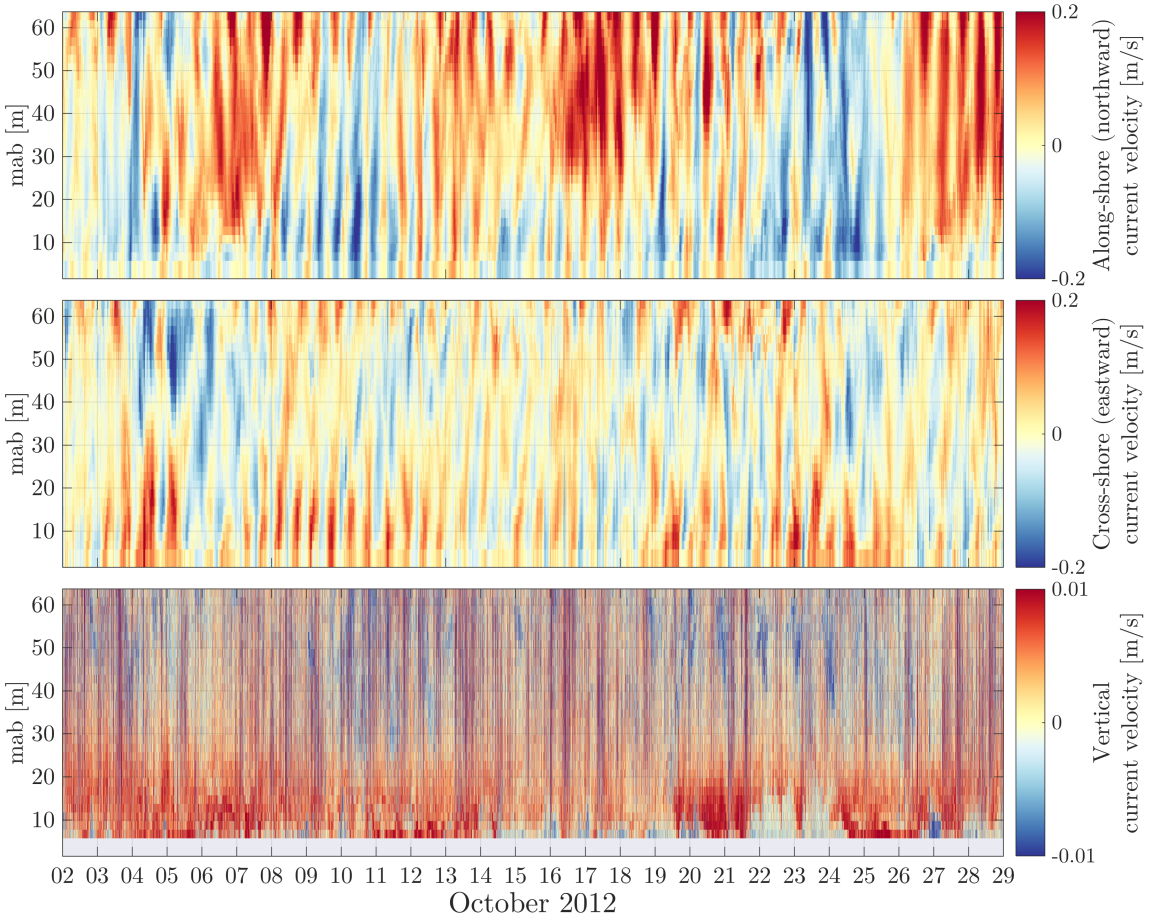

Figure 15. Along-shore (*u*; top), cross-shore (*v*, mid) and vertical (*w*; bottom) current velocity fields measured by the ADCP.

To extract the signal of the semi-diurnal internal-tide from the current velocity fields I performed a time-domain EOF decomposition of the rotated ADCP dataset. The first mode of the time-domain EOF decomposition of along-shore currents explained 60% of the variance and exhibited a barotrophic vertical structure. Spectral analysis of this mode had one distinct peak on the semidiurnal band (Figure 17) and the mode correlated with M_2 surface tide height (r=0.4 at 1.5 hr lag). The second EOF mode explained 19% of the variance and had a distinct mode-1 baroclinic vertical structure.

The spectral energy of the second mode was also focused in the semidiurnal band (Figure 17), however the mode was found to be de-correlated from the M_2 surface tide. This likely represents the influence of the semidiurnal internal tide, which exhibits periodic forcing but is typically de-coupled from the semidiurnal surface tide as a result of the distance from the internal tide generation site (Nash et al., 2012).

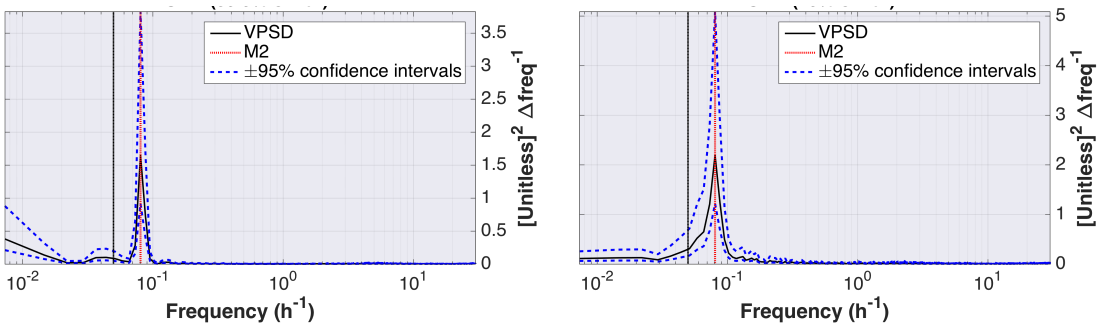

Figure 16. Variance-preserving power spectral density (PSD) of the first (left panel) and second (right panel) EOF modes of along-shore currents, presented along with 95% confidence intervals. The variability is most energetic at the M2 semidiurnal tidal frequency shown as vertical dashed red line.

The first EOF mode of the cross-shore current captured 40% of the variance, and similarly to the second mode of the along-shore current, exhibited a distinct mode-1 baroclinic vertical structure (Figure 18a). Here too spectral energy was centered over the M_2 frequency (Figure 18c) and the mode was de-correlated from the M_2 surface tide. The amplitude of the first EOF mode was variable in time, peaking during periods of upwelling, with weaker fluctuations during periods of downwelling (Figure 18b). The second mode captured 25% of the variance and was similar in character to the first mode of the along-shore current component.

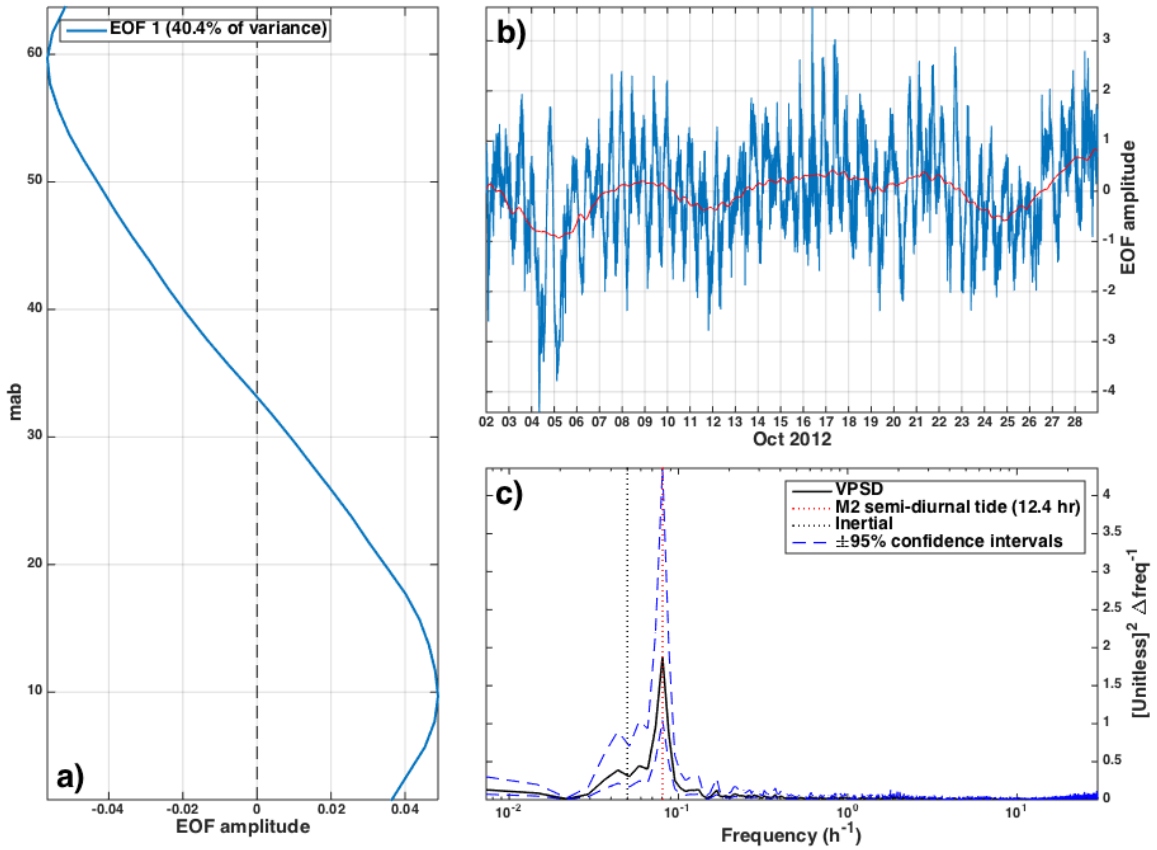

Figure 17. EOF decomposition of cross-shore velocities during 2012 study. (a) The first vertical mode captures 40% of the variance. (b) The temporal amplitude of the first mode is dominated by variability at the M2 frequency (c). This representation demonstrates the mode-1 nature of the internal tide and shows the variability in the strength of the internal tide during the experimental period, peaking around 4-5 and 16 October.

The second EOF mode of the along-shore current and first EOF mode of the cross-shore current will be referred to as the M_2 internal tide hereafter. Although secondary in importance to the processes discussed here, other products of the EOF analysis (e.g., vertical current components and other modes) are given in Table 4 and illustrated in Appendix B and Appendix C.

Table 4

EOF modes of currents velocity fields - fall 2012

	along-shore currents (v)		cross-shore currents (u)		vertical currents (w)	
Mode	Variance explained	Accumulated variance explained	Variance explained	Accumulated variance explained	Variance explained	Accumulated variance explained
1	59.8%	59.8%	40.4%	40.4%	54.7%	54.7%
2	18.9%	78.8%	25.1%	65.5%	9.7%	64.4%
3	7.8%	86.6%	12.3%	77.8%	6.0%	70.5%
4	4.4%	91.1%	7.1%	85.0%	3.5%	74.0%

Observations of Suspended Particulate Matter in the Water Column

Observations from the profiler and optical peak algorithm. Throughout the 4-week observation period, records from the profiler revealed the frequent presence of SPM layers with peaks well above the seafloor, overlying clearer water (Figure 19). Out of 667 profiles collected in 2012 study, the optical peak algorithm (designed to detect detached peaks in individual profiles) successfully identified 313 (46.9%) detached SPM peaks (Table 4). Similar to the findings of Cheriton et al. (2014) from fall 2011, the peaks centered approximately 10-20 m above the bottom (Figure 20), and at times, exhibited apparent semidiurnal variability. A summary of the algorithm outputs is given in Table 5.

Near the bottom (0.4 mab), measurements of turbidity indicate variability in the presence of an SPM rich bottom nepheloid layer (BNL; Figure 19b). Although there seemed to be correspondence between beam attenuation readings from the BNL and measurements from the mid-water column during high attenuation events (8 October and

15-18 October; Figure 19), only weak correlations were found between the records (r_{max}=0.33 at 24 hr lag).

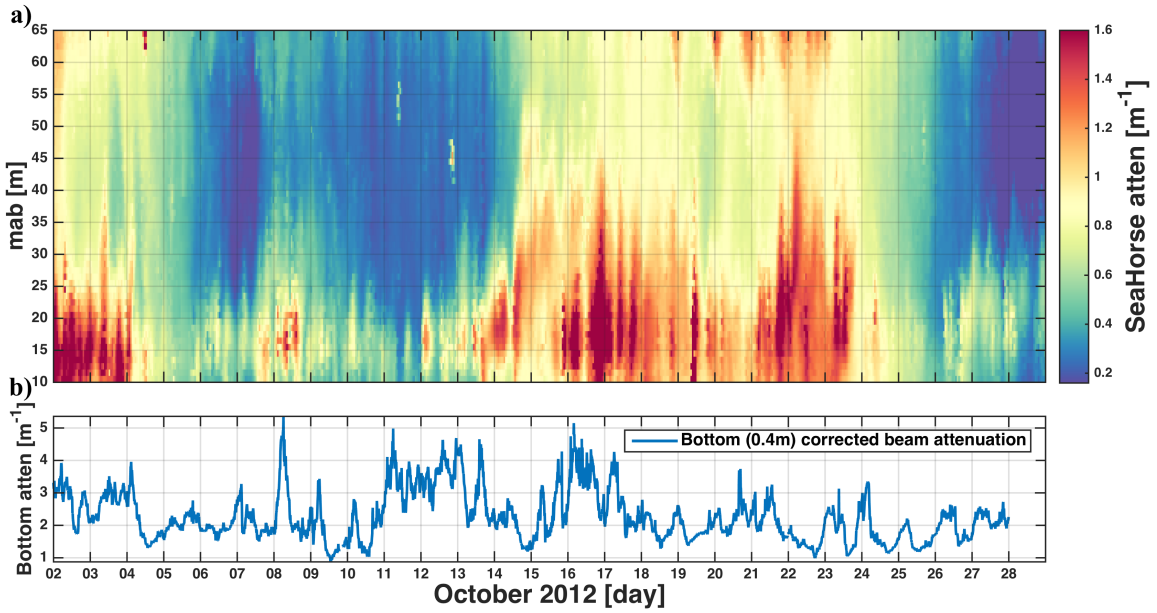

Figure 18. (a) Observations of SPM in the water column by the profiler and (b) near the bottom at 0.4 mab. High attenuation events are evident throughout 2-4, 8 and 12-24 of October.

Table 5

Results from optical peak algorithm - fall 2012

Detached SPM peak	Not detached	Rejected*	Mean beam attenuation anomaly (m^{-1})†	Mean height above bottom (mab)†	Mean detachment ratio (At_{ratio})†
294 (44.1%)	362 (54.2%)	11 (1.6%)	0.7 ± 0.03	17.7 ± 0.44	0.48 ± 0.02

*Rejected profiles did not meet basic criteria for analysis.
†±standard error to the mean (α=0.05).

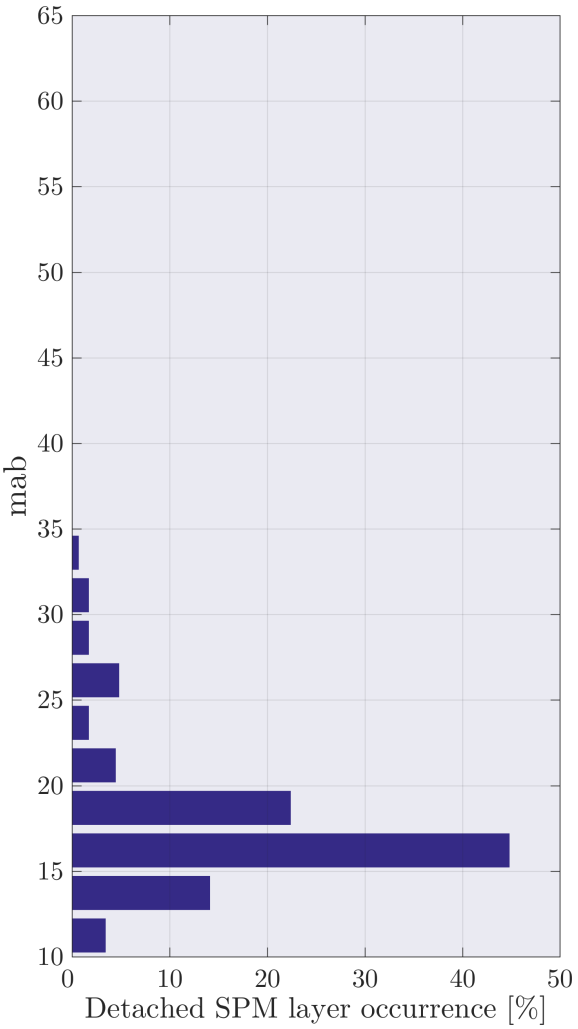

Figure 19. Vertical distribution of detached SPM layer peaks during the 2012 study period as identified by the optical peak identification algorithm.

EOF analysis of profiler beam attenuation records. I performed a time-domain EOF analysis of the profiler corrected beam attenuation records to examine the vertical structure of the variance within the observed SPM features in the water column and isolate the time scales associated with oscillations in detached peaks. Results of the EOF analysis are given in Table 6 and Figures 21-23. I focused attention on the first two modes, which explained the majority of the variance (93.8%).

Table 6

EOF modes of profiler corrected beam attenuation records - fall 2012

Mode	Variance explained	Accumulated variance explained
1	86.4%	86.4%
2	7.4%	93.8%
3	3.1%	97.0%
4	0.84%	97.8%

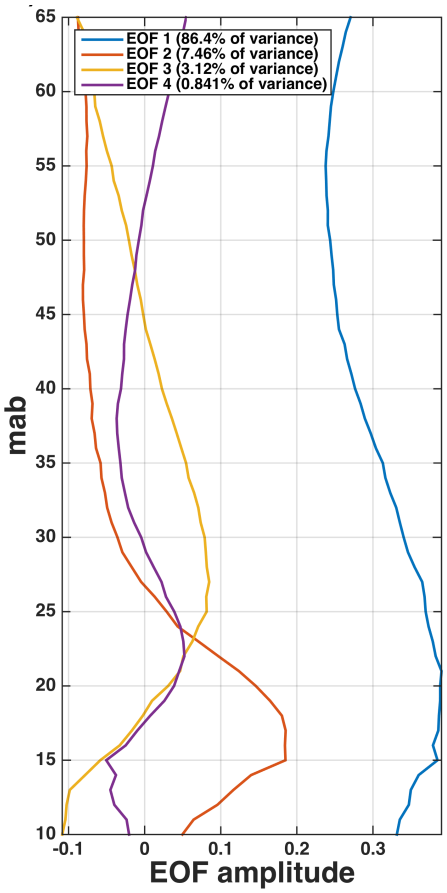

Figure 20. Vertical structures of EOF amplitude from the first 4 modes of corrected beam attenuation records from 2012.

The first EOF mode accounted for ~86% of the variance in the dataset and described the low-frequency temporal fluctuations of SPM in the water column. The vertical structure of the first mode was mostly uniform throughout the water column with

an increase in amplitude at ~15-20 mab (the same height detached SPM layers were centered at; Figure 21) fallowed by a decrease towards the bottom of the profile. The time-domain spectral energy of the first mode of variability was dominated by low frequency fluctuations (1-2 week; Figure 22a) following oscillation patterns found in wave and wind records (Figure 23a). The vertical structure of the second EOF mode was similar in character to structure of detached SPM layers seen in individual profiles (Figure 21) and carried a strong semidiurnal tidal signal of M_2 frequency (Figure 22b). The second mode also contained a considerable amount of variance in 3-5 day bands.

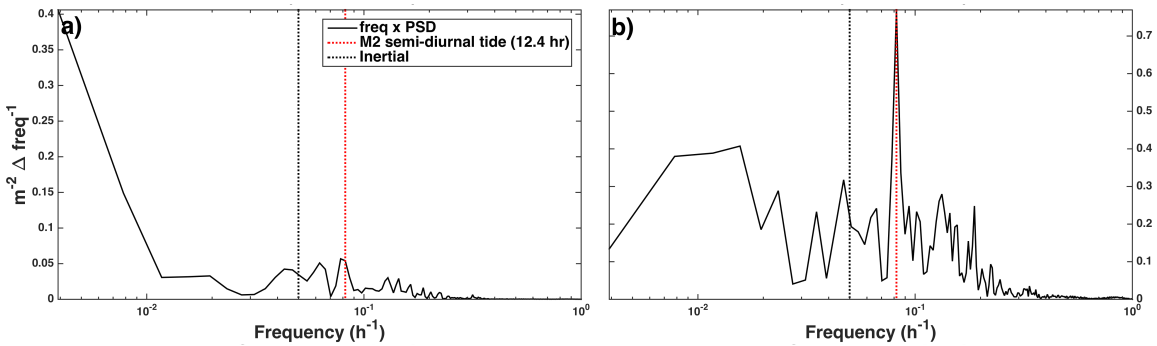

Figure 21. Variance-preserving spectral analysis of the first (a) and second (b) EOF modes of corrected beam attenuation records from the fall 2012 study period. Inertial (*f*) and M_2 frequencies are shown as vertical dashed lines.

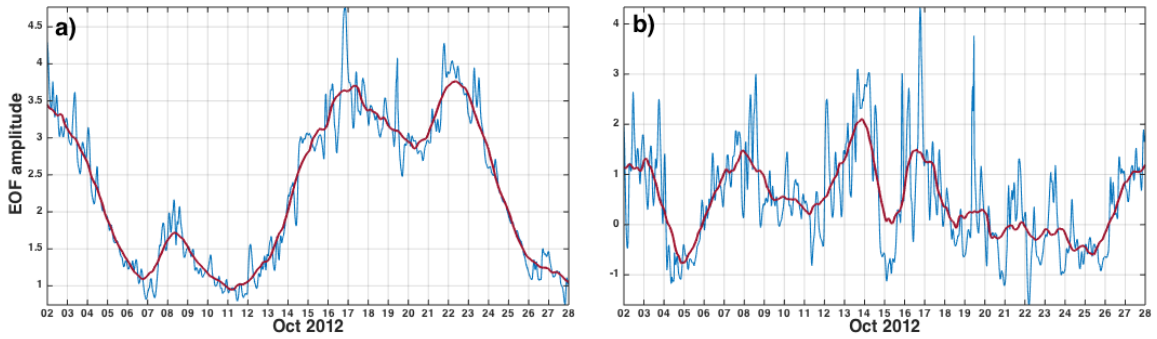

Figure 22. Time-domain representation of the first (a) and second (b) EOF modes of variability computed from corrected beam attenuation records collected in 2012. Red line indicates the sliding mean of 6 semidiurnal cycles.

Suspended Particle Trajectory Simulation

I simulated the horizontal and vertical excursions of detached SPM layers over the southern Monterey Bay shelf by tracking the movement of theoretical particles starting at the depths and times of SPM peaks as identified by the optical peak algorithm. For each ‘‘particle’’ I assigned a range of sinking velocities, from the Stokes sinking velocity for 34 μm particles (7×10^{-4} m s^{-1}) to the estimated sinking velocity for large 250 μm flocs (4×10^{-3} m s^{-1}) (Sternberg et al., 1999). A detailed description of this simulation is found in methods section 5.5.

The backwards-in-time portion of the particle tracking model simulated a point of origin for all of the particles that were tested (n=294). In most cases, the vertical velocities preceding the appearance of detached SPM layers at the profiler site were sufficient to not only counteract the estimated settling velocity, but to also deliver the SPM from the seafloor up to the depth observed at the profiler site within a relatively short time frame (mean was 4.3 ± 0.52 hours, α=0.05). Corresponding to these time scales, and in agreement with estimates by Cheriton et al. (2014), the horizontal excursion of modeled particle origin proved to be surprisingly close to location of the study site spanning only ~1 km on average (well within the mudbelt range; Figure 24).

Once the modeled particles reached the mid-water column (at the study site), vertical transport (6-min averaged ADCP measurements) was generally matched the vertical movement of isotherms. Averaging the vertical placement of the simulated particles closely reproduced the vertical distribution of the detached SPM layers recorded by the profiler (Figure 25a). The vertical distribution of simulated particle trajectories

that did not take into account flocculation ended up in shallower parts of the water column (Figure 25a), suggesting that flocculation influences the vertical distribution of SPM carried in these layers.

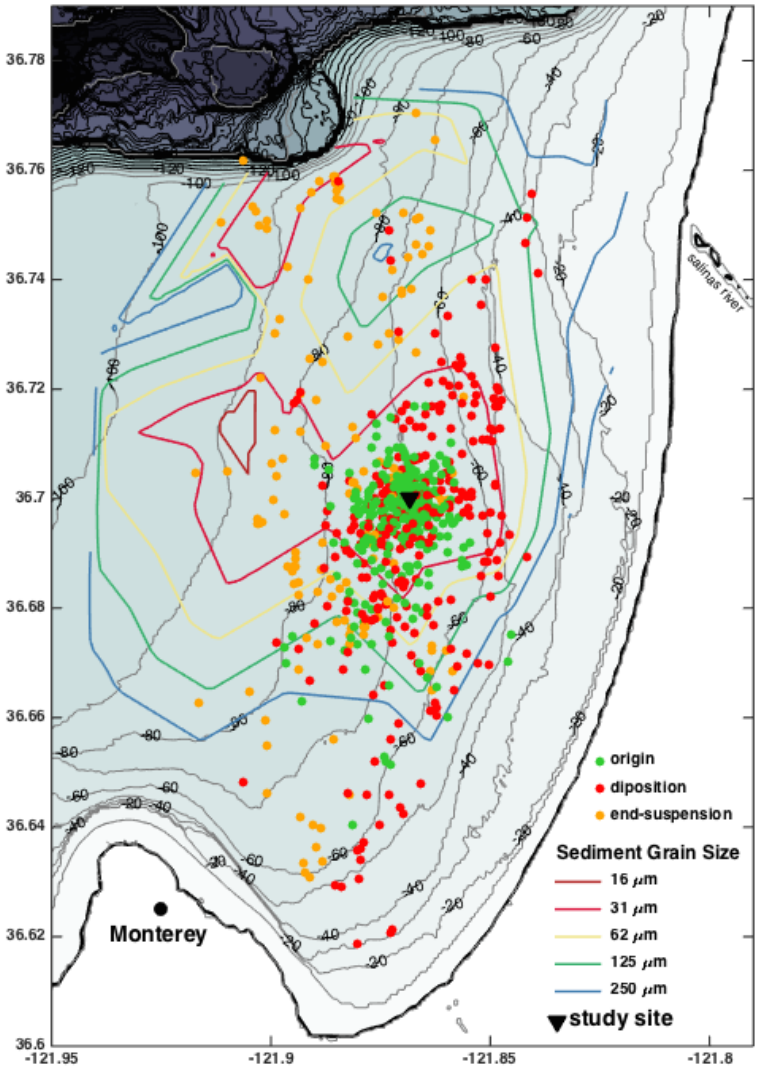

Figure 23. Origin (green dots) and fate (red and orange dots) of particle trajectory simulation (flocculation scenario) superimposed over the southern shelf of Monterey Bay. Colored contours indicate the distribution of sediment grain sizes across the shelf as shown in the map's legend. The origin of the majority of particles traced back to within the mudbelet ~1 km around the study site (black triangle).

Forward-in-time particle trajectories were long lasting as particles reached mid-water depths "riding" upward vertical velocity bursts. In the case where no aggregate settling velocity was applied, modeled particles were advected to the ocean's surface in some cases and only 23.7 % were deposited back to the bed within the 24-hour time frame of the forward model. Introducing aggregate settling velocities increased the number of deposited particles to 35.9 %, and decreased the average suspension time from 23.3 hours in when no aggregate settling velocity was applied to 21 hours for aggregated particles. In both cases, the majority of particles remained in suspension beyond the model's 24-hour forecasting limit.

Based on the horizontal trajectories across the shelf I computed a general evaluation of the mudbelt's stability by comparing the origin and end coordinates of modeled particles with the know location of the mudbelt (Figure 24). The majority of trajectories simulated under the aggregating scenario placed erosion and settling (start and finish) within the mudbelt bounds (41%) with a secondary exportation trend in ~21% of profiles (Figure 25b). The simulation of particle horizontal advection distributed particle fates equally across isobaths with a slight on-shore trend. This minor instability of the mud belt found by the model is in agreement with other sources in the literature, which identify the study period as the beginning of the mudbelt's mobilization period (Storlazzi et al., 2007).

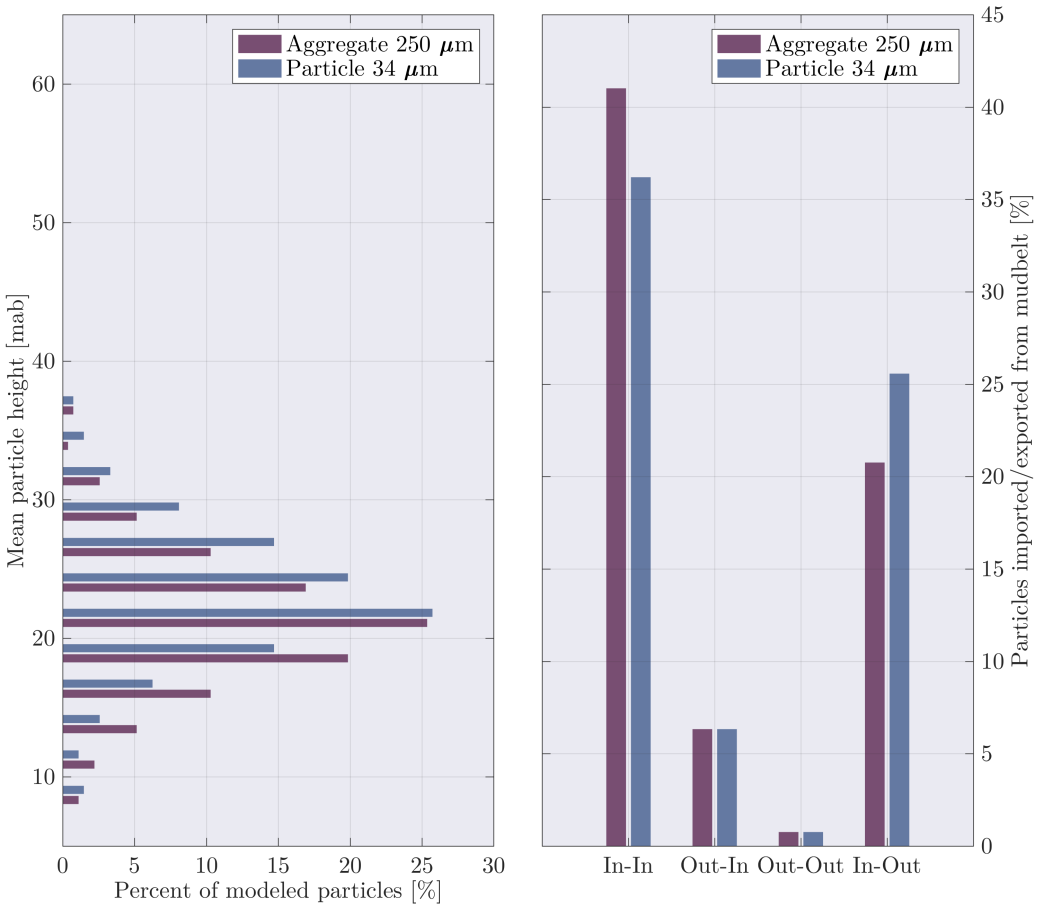

Figure 24. Mean vertical distribution of simulated particle trajectories (a) and mudbelt erosion and deposition trends (b) determined according to particle trajectory origin and fate (e.g., In-In (Out-Out) means that particles originated and deposited from within (out) of the mud belt).

Processes Associated with Detached SPM Layers

Bottom shear stress from currents and waves. Similar to Cheriton et al. (2014) analysis of 2011 data, I found orbital velocities from surface waves to be the dominant component of frictional bottom shear stress over the mid-continental shelf during fall 2012. During the period of observation surface wave-driven bed shear stress (or simply τ_w hereafter) exceeded the bottom stress driven by horizontal near-bed currents (τ_c) 84.7 % of the time (Figure 26a). However, τ_w alone managed to exceed resuspension

thresholds for D_{50}=34 µm grain sizes only in a few energetic wave events (Oct 14-18). While τ_c alone very rarely managed to exceed the resuspension threshold (<1 % of the time), currents played an important part in that when combined with surface wave orbital velocities, the resulting bottom shear stress often surpassed critical thresholds needed for resuspension of fine sediment (e.g., Oct 10-13 and Oct 24; Figure 26a). Overall, during this 4-week period, combined wave-current shear stresses (τ_{wc}) surpassed the critical threshold (τ_{cr}) 13.2% of the time for grain sizes of D_{50} = 34 µm and 47.7 % of the time for grain sizes of D_{25} = 14 µm.

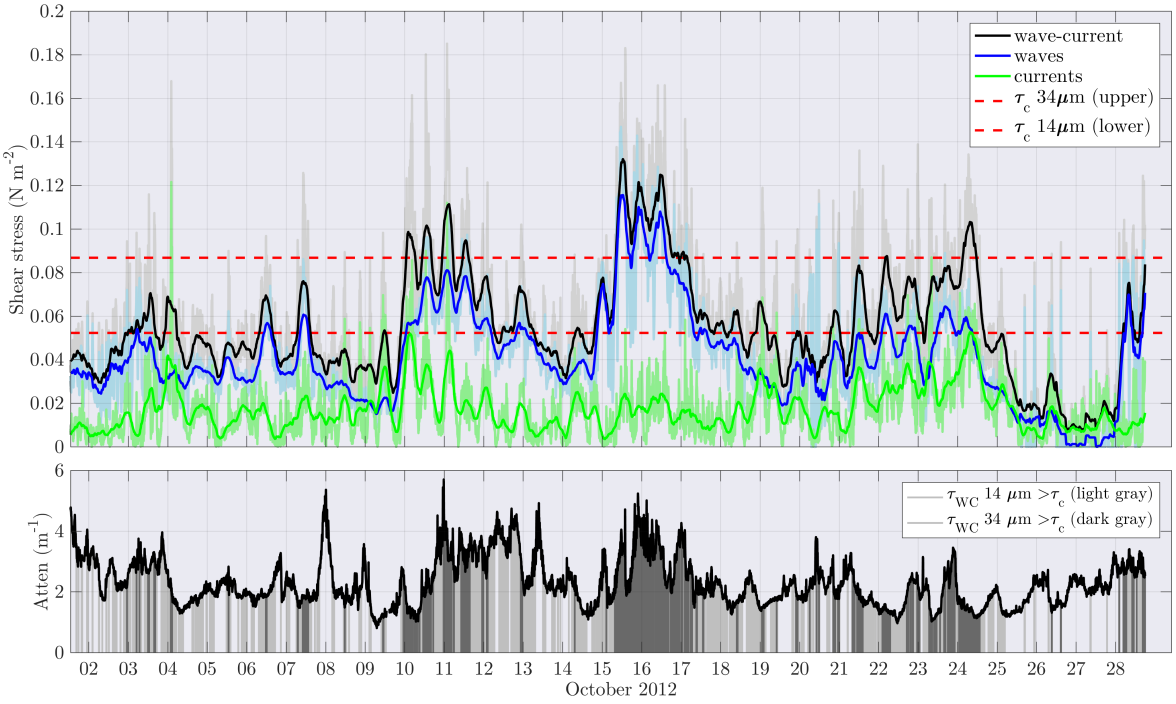

Figure 25. (a) Smoothed bed shear stresses form combined wave-current (black line), surface wave-only (blue line), and current-only (green line) stresses. Raw signal is shown in faded color in the background. The critical shear stress threshold for grains of diameter 34 µm (upper) and 14 µm (lower) are overlaid (red dashed lines; τ_{cr} = 0.08 N m^{-2}). (b) Near bottom beam attenuation (0.4 mab), with times when combined wave-current bed shear stresses exceeded the critical threshold indicated by the light gray (14 µm) and dark gray (34 µm) shaded regions.

In addition to estimates of τ at the study site, I computed spatial estimates of τ_w for the study period of fall 2011 based on buoy CDIP 156 wave data under the assumption of a uniform surface-wave field across the area of the southern Monterey Bay shelf. In addition, for the purpose of this analysis I assumed an even grain size distribution of D_{50}=34 μm over the entire shelf. It is important to note that although some regions of the shelf consist of grain size distributions spanning much higher grain diameters (recall Figure 2), increased grain diameters result in higher hydraulic roughness of the bed, which in turn yield higher shear (Eisma, 1993), and so the spatial estimates of bed shear stress produced by this analysis represent lower-bound conditions.

The estimates of τ_w were computed for depths ranging 20-100m, then hourly averaged, and finally, assigned to a spatial grid of corresponding depths obtained from bathymetry data of the Monterey Bay (MBARI). Results of the spatial analysis shown in Figure 27 reflect spatial variations dictated mostly by the sloping topography of the continental shelf; this is expected given the decaying nature of surface-wave orbital velocities as depth increases. The average of τ_w calculated for the entire 4-week duration of the study periods is shown in Figure 27a and peak τ_w conditions are shown in Figure 27b.

For reference, I repeated the analysis of τ_w for the fall 2011 field campaign. During 2011 study period, levels of τ_w were higher than in 2012 and surface waves strong enough to affect the mudbelt (60-90m) were more frequent. Although the 2011 deployment was only a week longer, six large surface wave events took place (24-27, 28-30 September and 4-5, 6-8, 12-15, 26 October) compared to two in 2012 (16-18 and 21-

25 October; Figure 28a, b). These differences were most pronounced in deeper regions of the shelf where τ_w at 70 m exceeded τ_{cr} 22.2% of the time in 2011 versus 6.3% in 2012 (Figure 29). For comparison, time-series of τ_w estimates for 50, 70 and 90m for both deployments are shown in Figure 28.

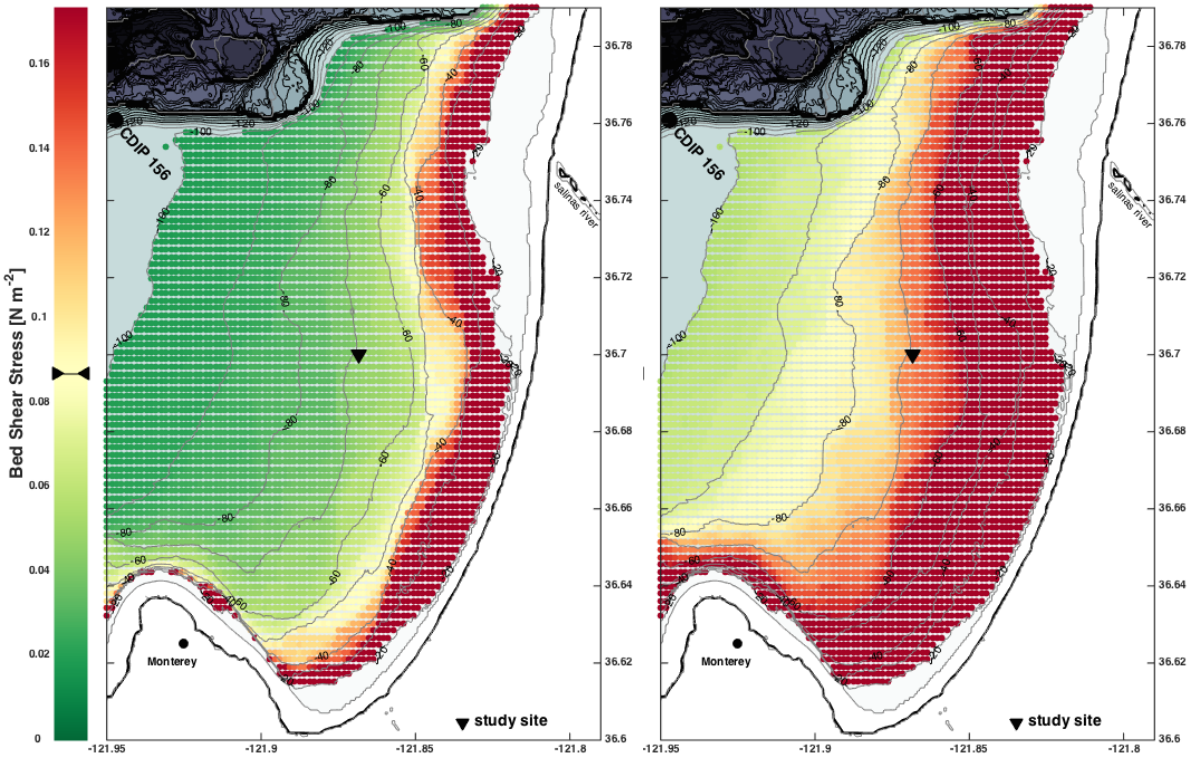

Figure 26. Spatial estimates of τ_w over the southern shelf of Monterey Bay. The magnitude of τ_w is indicated by color-bar and the critical threshold for resuspension τ_{cr} is shown (black markers on colorbar). (a) Average τ_w conditions over the entire period of observation (October 2012) and (b) peak τ_w conditions (15 October, 2012 17:00 PST) are shown.

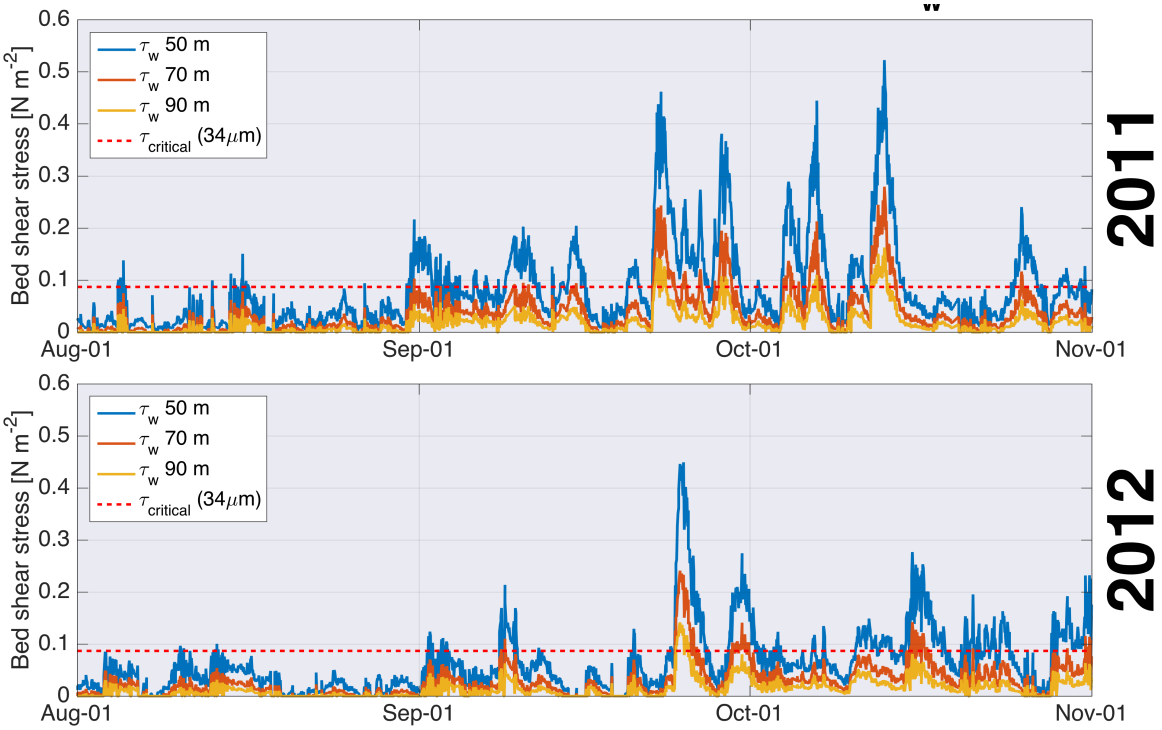

Figure 27. Modeled time-series of τ_w estimates at 50, 70 and 90 m form 2011 (a) and 2012 (b). Black arrows indicate high bed shear events where $\tau_w >>> \tau_{cr}$.

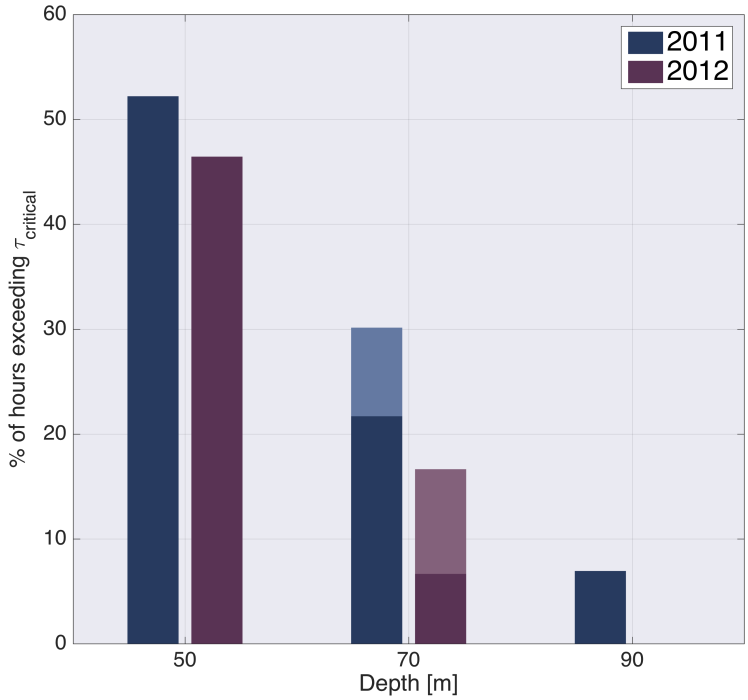

Figure 28. Times where $\tau_w > \tau_{cr}$ are shown in % of total duration of each deployment at 50, 70 and 90 m shelf depths. At 70m, light colored bars show estimates of τ_{wc}, which were available due to current measurements at the study site.

Bottom shear stress forcing of detached SPM layers. My analysis of the relationship between total frictional bottom shear stress τ_{wc} calculated for the study site and SPM concentration in the BBL (i.e., near bottom beam attenuation; Figure 26b) yielded a weak cross-correlation coefficient (r = 0.16). However, when examined more directly at an event scale, the relationship became clearer in events forced strongly by τ_w (i.e., Oct 14-18, r = 0.6) and less clear in events where shear stress was mutually forced by τ_w and τ_c (i.e., Oct 10-13, r = -0.12).

To assess the relationship between SPM concentrations carried in the mid-water column and τ_w, I first computed a 10-m depth-bin average of corrected beam attenuation measurements collected by the profiler centered at 17 mab (~the height where most detached peaks were seen). Then, I performed a lagged cross-correlation analysis between the corrected beam attenuation signal for 17 mab and τ_w estimated for shelf depths of 50, 70 and 90 m to examine the possibility of a delayed response due to advection and diffusion of SPM from the bottom. Lagged cross-correlation coefficients increased in significance as depth shoaled and peaked at 50 m with a time lag of ~12 hours (r=0.54; Figure 30); inferring a strong (and statistically significant) connection between particles sheared from the bottom at shallow depths and mid-water-column SPM concentrations at the study site (70 m).

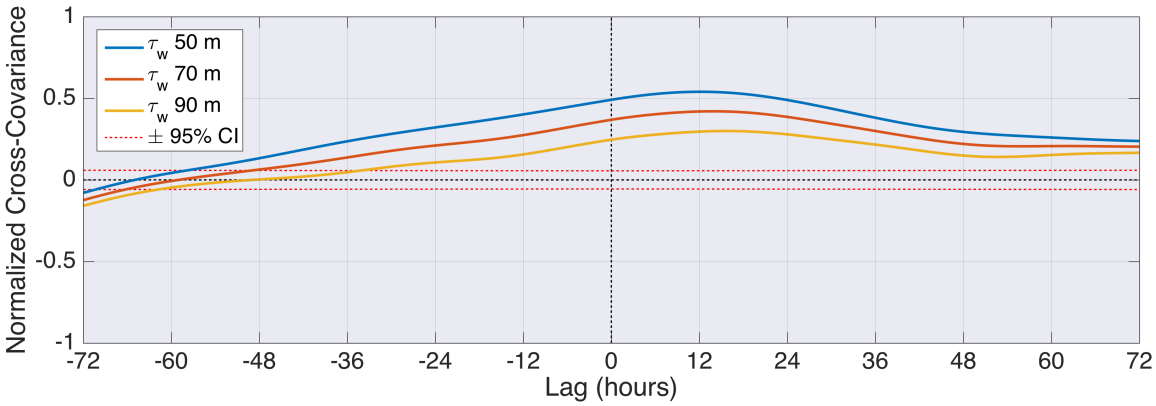

Figure 29. Normalized cross-covariance illustrating the lagged relationships between wave-induced bed shear stress τ_w at various depths and concentrations of SPM at 17 mab. The 95% confidance intervals are indicated by red dashed lines.

Semidiurnal internal-tide forcing of SPM features. I performed 2D wavelet analysis of the M_2 frequency band to examine the connection between the M_2 internal tide (i.e., mode-1 EOFs) and SPM concentrations in the mid-water column over time and vertical space. In this analysis, I used a 6-day running window to extract subsets of the time-series for processing and generated a new time-series made of the calculated data products (Figure 31).

Over the period of observation energetic perturbations by the M_2 frequency were pronounced during high attenuation events (e.g., 15-20 October 2012) in which reoccurring detached SPM layers were seen (Figure 31). The vertical structure of time-integrated M_2 spectral density generally matched the vertical distribution of detached SPM peaks detected by the optical peak algorithm (Figure 32).

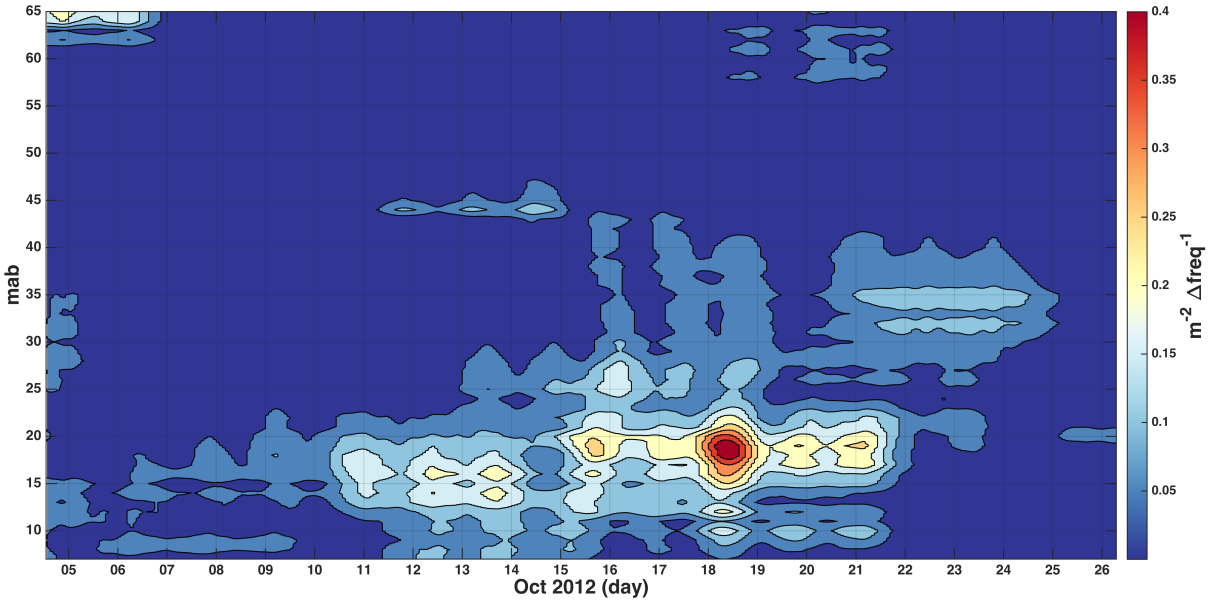

Figure 30. Wavelet analysis of the M_2 frequency band in SPM concentrations. M_2 frequency is most energetic during high attenuation event 15-20 October.

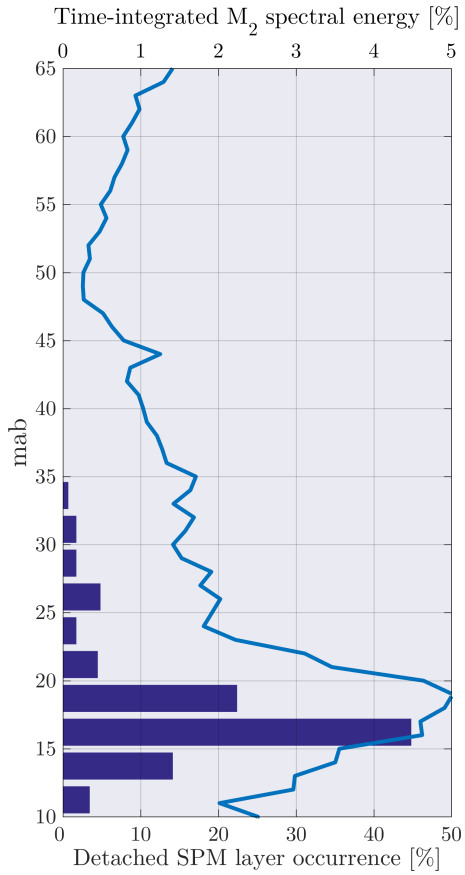

Figure 31. Time-integrated vertical structure of M_2 spectral density extracted from SPM concentration records (top x-axis). Vertical structure matched the vertical distribution of detached SPM peaks (bars) detected by the optical peak algorithm (bottom x-axis).

Logistic Regression Classification Model

To quantify the influence of τ_w and the M_2 internal-tide on the appearance of detached SPM layers, I fitted the time-series of τ_w and of M_2 under the logistic regression framework. The models produced under this analysis served a dual purpose: 1) to quantify the level of association between the appearance of detached SPM layer and the measurement variables (i.e., M_2 internal-tide, τ_w or both) using classification performance metrics, and 2) to establish a predictive classification model that returns the probability for observing a detached SPM layer given the measurement variables. The measurement variables were smoothed using a low-pass filter (<20 hour) and fitted against the binary record of detached SPM layers identified by the optical peak algorithm; profiles that included a detached SPM layer were defined as 1 versus 0 in their absence. Logistic regression models were fitted for each measurement variable individually and as an additive combination of the two using MATLAB's statistical toolbox.

To examine the possibility of a delayed response between the measurement variables and the appearance of detached SPM layers (due to the time scales associated with advection and diffusion of SPM from the bottom to the mid water column), I computed multiple logistic regression models for each of the proposed measurement variables over a range of time lags (0-24 hours) and then compared those models using the Akaike information criterion (AIC) statistic (Akaike, 1998). AIC is a measure of the relative quality of statistical models for a given set of data. Given a collection of models for the data, AIC estimates the quality of each model, relative to each of the other

models. Hence, AIC provides a means for model selection. The models that minimized the AIC statistic were selected for further analysis.

Using the method for model selection described above, I compared logistic regression models of the along-shore (v) and cross-shore (u) current components of the M_2 internal-tide decomposed from the EOF analysis. Similarly, I compared logistic regression models using τ_w estimates computed for 50 m, 70 m and 90 m. Out of those the cross-shore (u) current component of the M_2 internal-tide and τ_w computed for 50 m displayed the best performance and were selected for further analysis. Results for the model selection analysis are given in Table 7 and illustrated in Figures 33 and 36.

Table 7

Comparison of logistic regression models

	M_2 internal-tide		Surface-wave bed-shear-stress (τ_w)		
	along-shore (v)	cross-shore (u)	50 m	70 m	90 m
AIC	806.3	**772.7**	**803.2**	826.1	844.4
Classification accuracy	64%	**66%**	**66%**	66%	65%
Lag (hr)	9	**12**	**13**	12	12

*Selected models from each category are shown in bold text.

The derived logistic regression coefficients and model diagnostics for the selected models, as well as the additive combination of the two, are given in Tables 8-10 and illustrated in Figures 34, 37 and 39. The classification performance evaluation of the selected models via ROC curve along with ±95% bootstrapping confidence bounds (Macskassy & Provost, 2004) are illustrated in Figures 35, 38 and 40. Finally, a comparison of classification performance for all three models is given in Table 11 and illustrated in Figure 41.

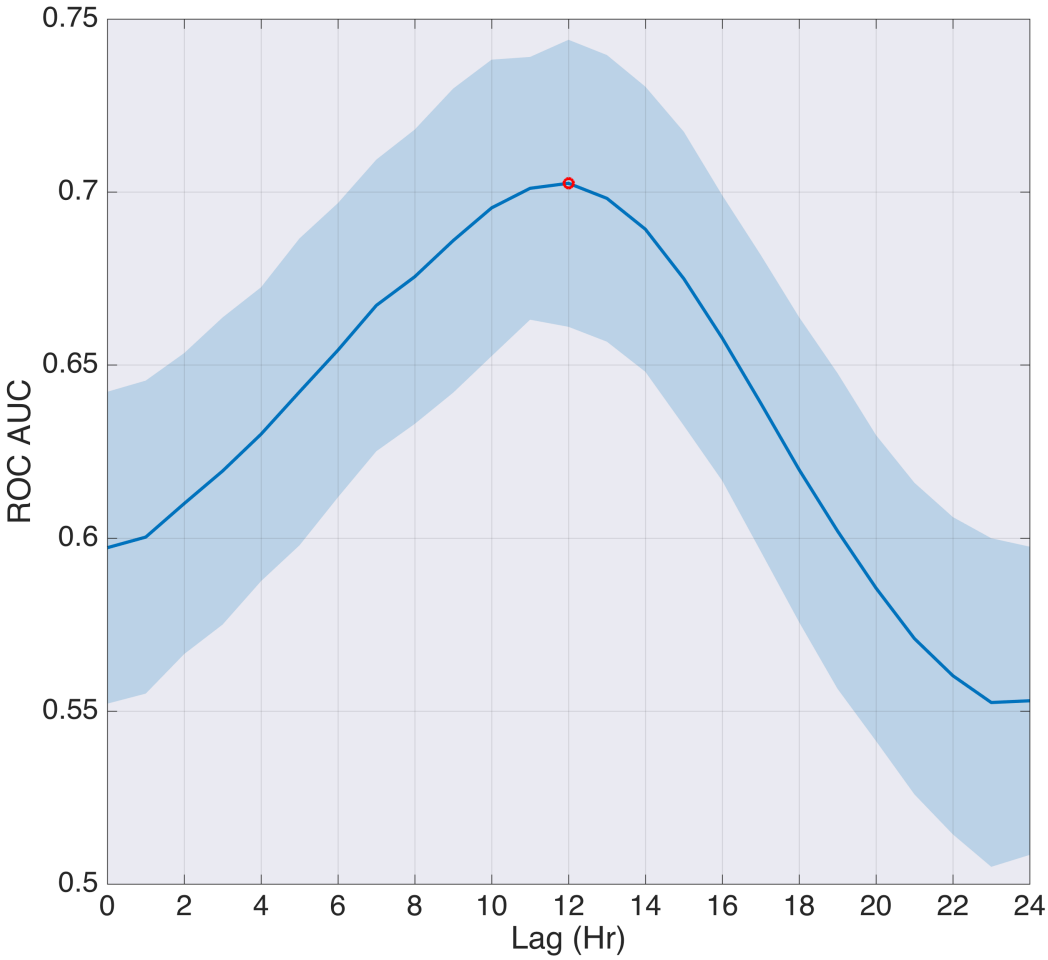

Figure 32. Analysis of classification performance using ROC for model comparison of the cross-shore (u) component of the M_2 internal-tide over varying lags (blue line), along with ±95% bootstrapping confidence bound (blue shaded area). The model that displayed the best classification performance (i.e., maximized AUC statistic) is indicated by red dot.

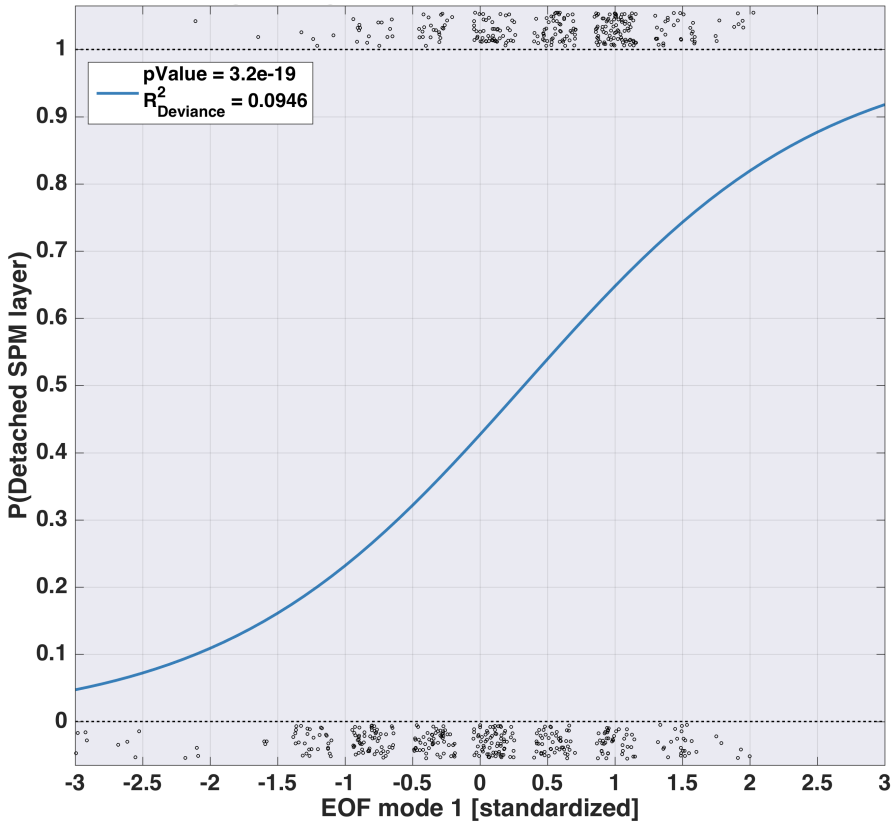

Figure 33. The derived Logistic sigmoid curve for cross-shore (u) component of the M_2 internal-tide. Binned data points (black dots) are also shown; the density of dots reflects the abundance of data in each bin.

Table 8

Logistic regression ($logit(y) \sim \beta_0 + \beta_1 x$) analysis of M_2 internal-tide (12hr lag)

	Estimate	SE	t-stat	p-value
Intercept (β_0)	-0.294	0.087	-3.367	7.6×10^{-4}
Slope (β_1)	0.903	0.112	8.021	1.0×10^{-15}
Model diagnostics				
	Deviance	DFE	χ^2 stat	p-value
$logit(y) \sim \beta_0$ $(Null)$	849.01	618		
$logit(y) \sim \beta_0 + \beta_1 x$	768.67	617	80.34	3.1×10^{-19}
R^2_{deviance}=0.09	AIC=772.66			

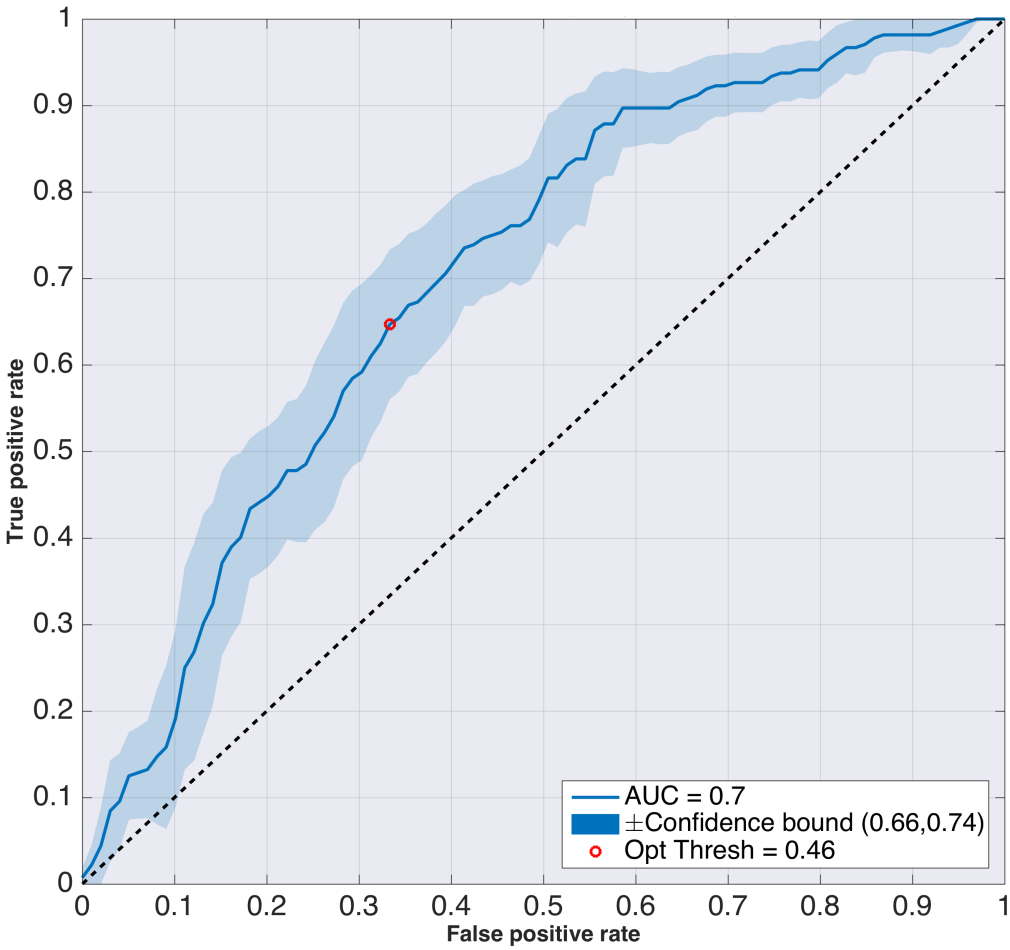

Figure 34. ROC curve for M_2 internal-tide (u) logistic regression model representing the accuracy of classification under varying probability thresholds (blue line), along with ±95% bootstrapping confidence bound (blue shaded area). The optimal operating point of the ROC curve (red dot) calculated using the ROC cost function is also shown.

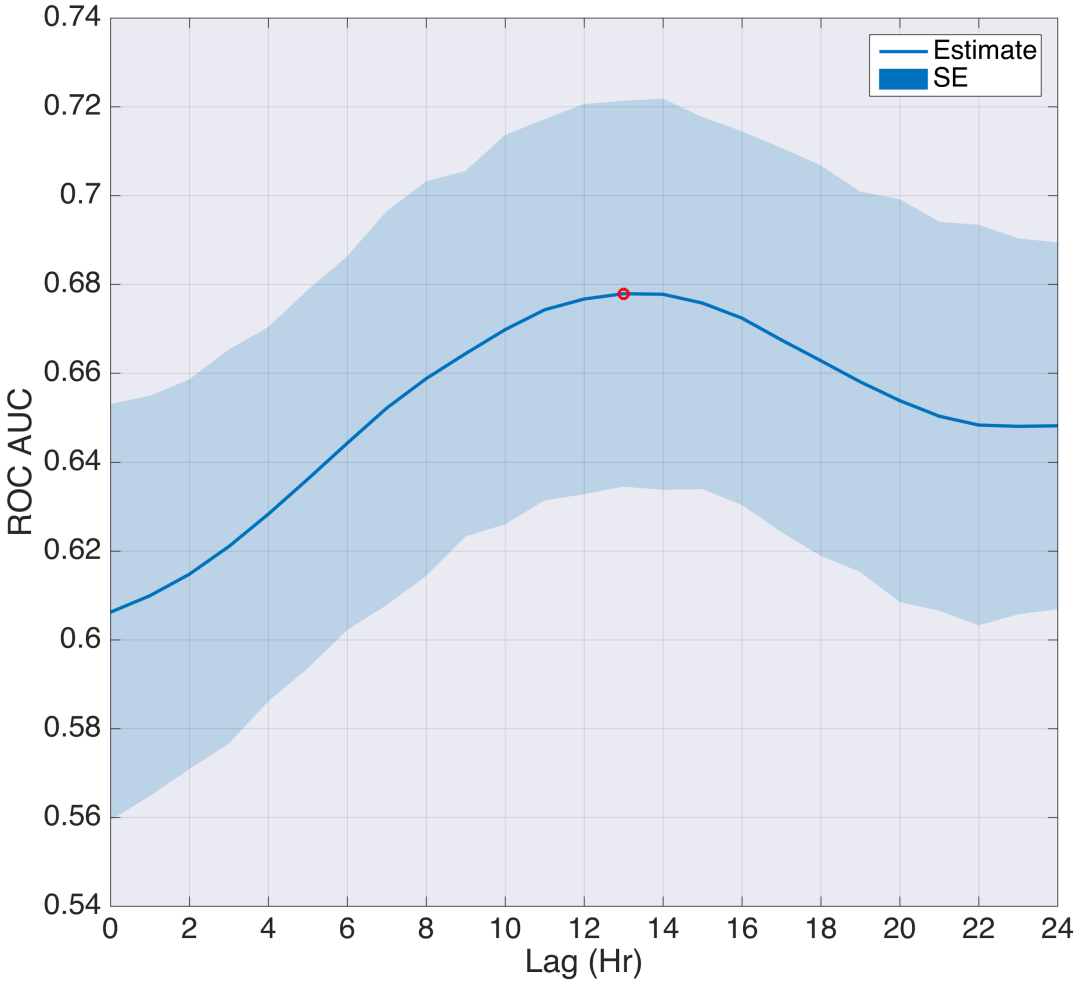

Figure 35. Analysis of receiver operating characteristic (ROC) curve for model comparison of τ_w (50 m isobath) over varying lags (blue line), along with ±95% bootstrapping confidence bound (blue shaded area). The model that displayed the best classification performance (i.e., maximized AUC statistic) is indicated by red dot.

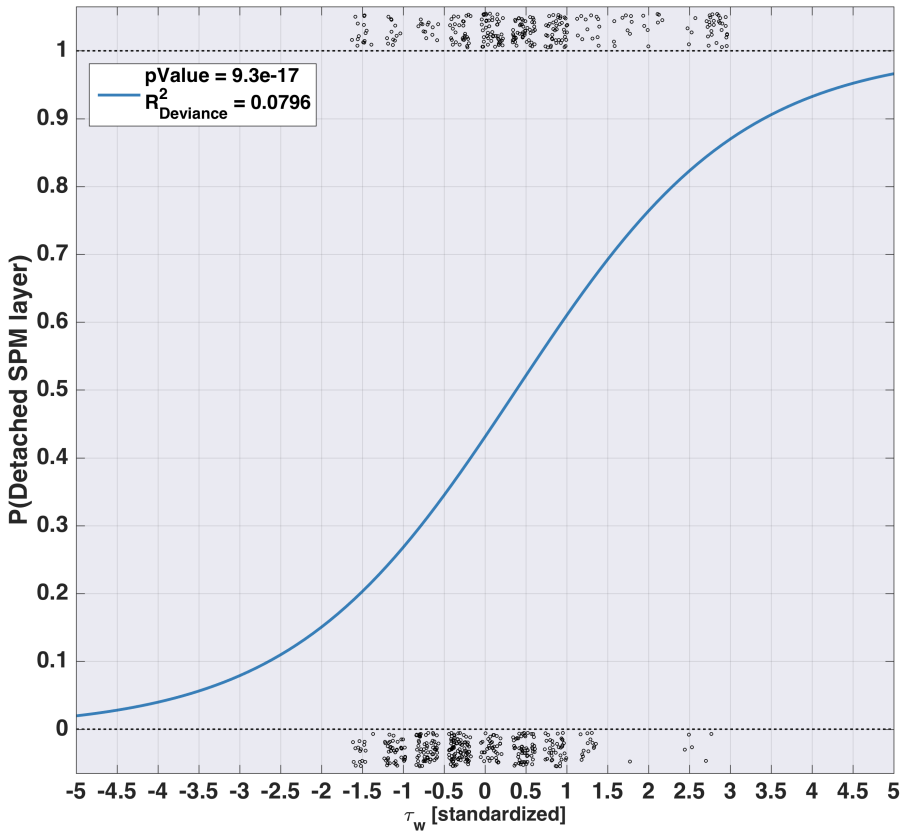

Figure 36. Logistic sigmoid curve for τ_w (50 m isobath). Binned data points (black dots) are also shown; the density of dots reflects the abundance of data in each bin.

Table 9

Logistic regression ($logit(y) \sim \beta_0 + \beta_1 x$) analysis of τ_w 50m (13hr lag)

	Estimate	SE	t-stat	p-value
Intercept (β_0)	-0.278	0.084	-3.286	1.0×10^{-3}
Slope (β_1)	0.726	0.096	7.539	4.7×10^{-14}
Model diagnostics				
	Deviance	DFE	χ^2 stat	p-value
$logit(y) \sim \beta_0(Null)$	868.34	634		
$logit(y) \sim \beta_0 + \beta_1 x$	799.23	633	69.10	9.3×10^{-17}
R^2_{deviance}=0.07	AIC=803.2			

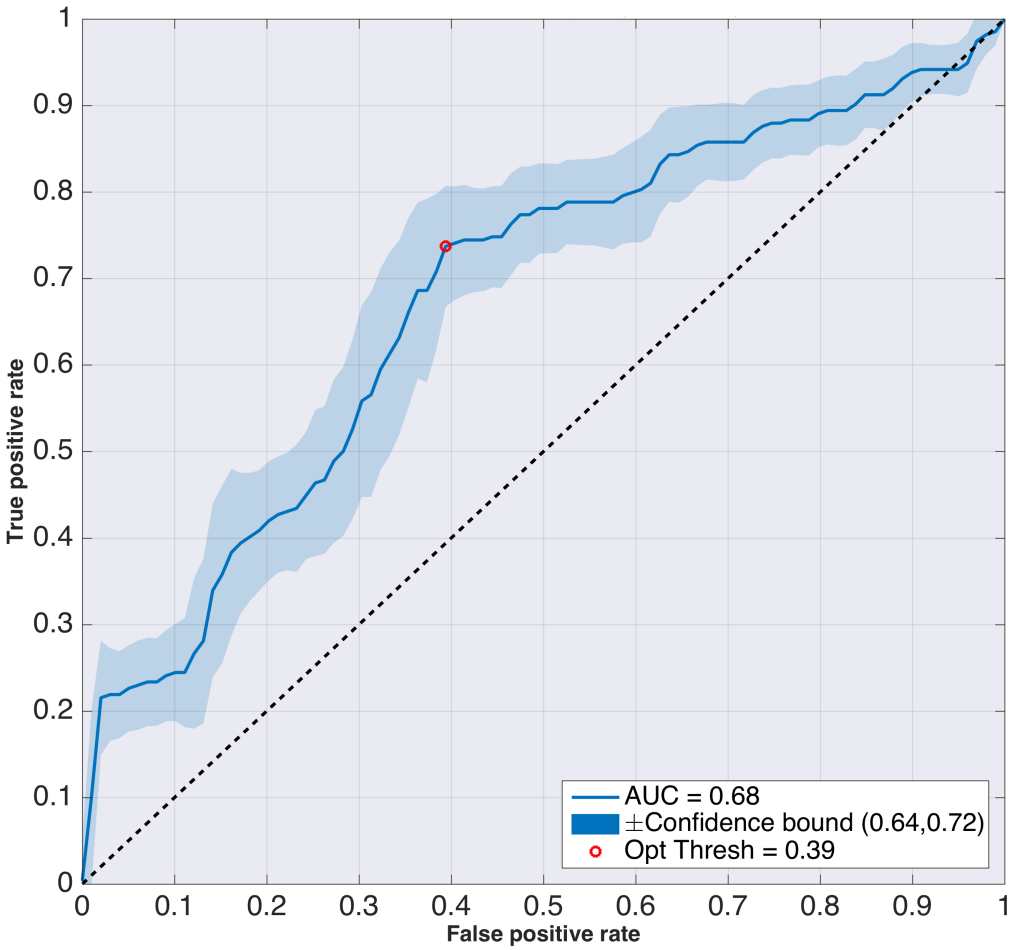

Figure 37. ROC curve for τ_w (50 m isobath) logistic regression model representing the accuracy of classification under varying probability thresholds (blue line), along with ±95% bootstrapping confidence bound (blue shaded area). The optimal operating point of the ROC curve (red dot) calculated using the ROC cost function is also shown.

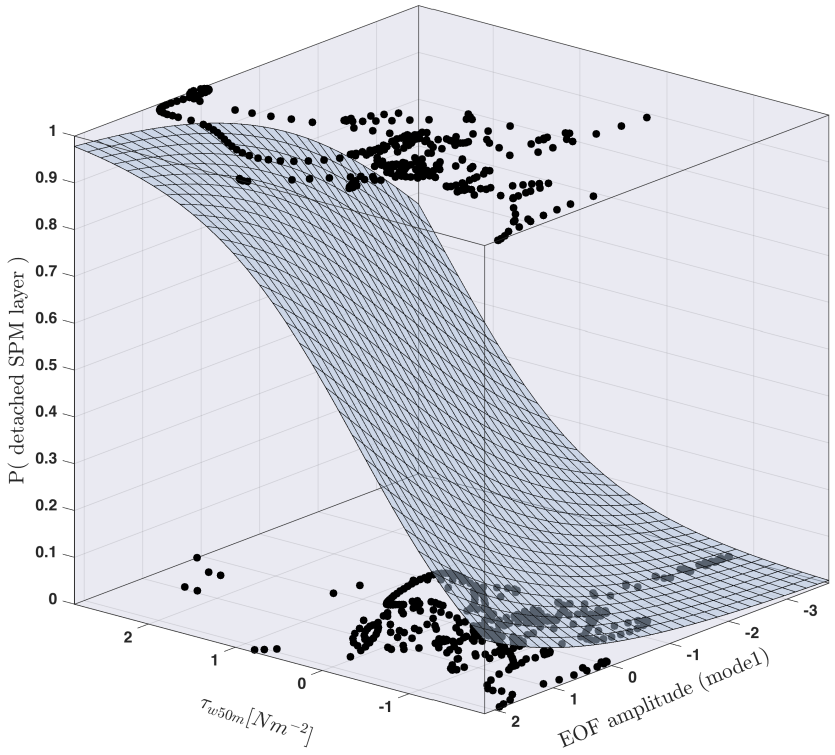

Figure 38. Logistic sigmoid surface for τ_w (50m) and M_2 internal-tide (u) additive logistic regression model. Data points used for analysis (black dots) are also shown.

Table 10

Additive logistic regression ($logit(y) \sim \beta_0 + \beta_1 x + \beta_2 x$) analysis of τ_w (13hr lag) and M_2 internal-tide (12hr lag)

	Estimate	SE	t-stat	p-value
Intercept (β_0)	-0.333	0.091	-3.654	2.5×10^{-4}
Slope (β_1) - τ_w (50 m)	0.735	0.102	7.197	6.1×10^{-13}
Slope (β_2) – M_2 internal-tide (u)	0.926	0.116	7.964	1.6×10^{-15}
Model diagnostics				
	Deviance	DFE	χ^2 stat	p-value
$logit(y) \sim \beta_0(Null)$	883.96	644		
$logit(y) \sim \beta_0 + \beta_1 x + \beta_2 x$	731.73	642	152.23	8.7×10^{-34}
R^2_{deviance}=0.172	AIC=737.7			

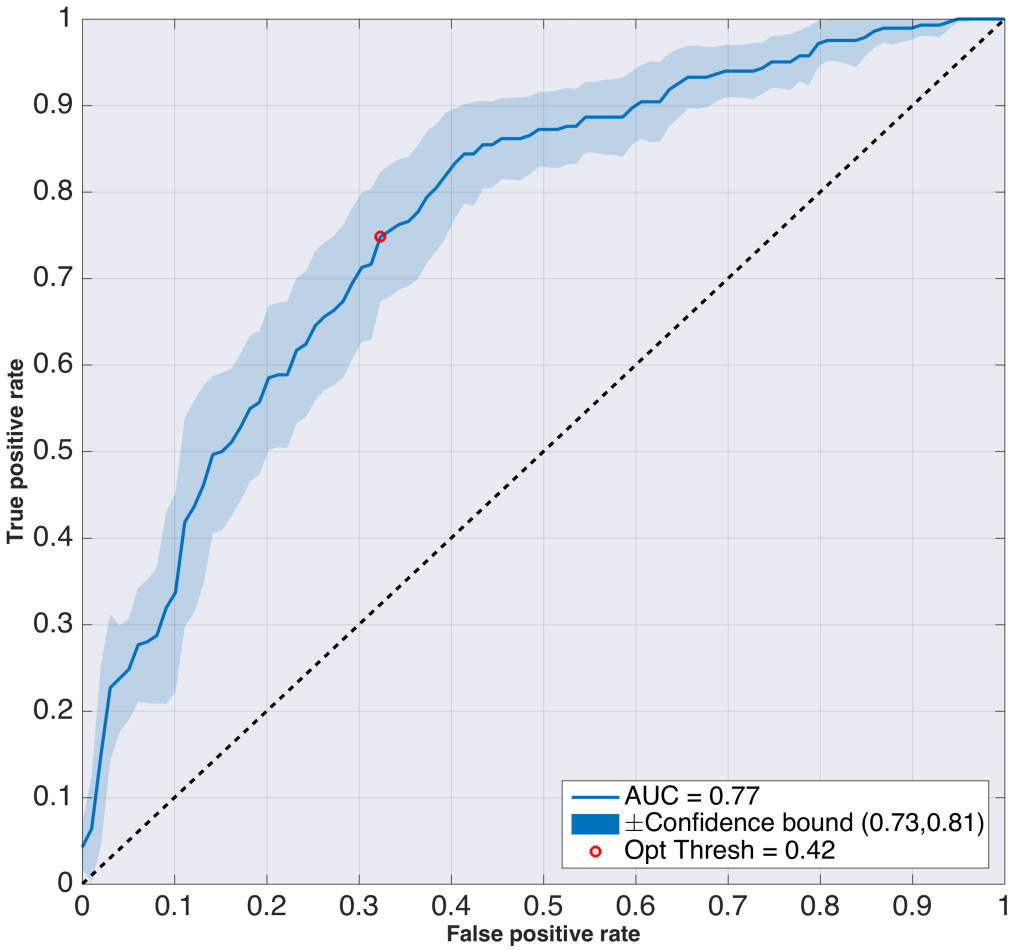

Figure 39. ROC curve for τ_w (50m isobath) and M_2 internal-tide (u) additive logistic regression model representing the accuracy of classification under varying probability thresholds (blue line), along with ±95% bootstrapping confidence bound (blue shaded area). The optimal operating point of the ROC curve (red dot) calculated using the ROC cost function is also shown.

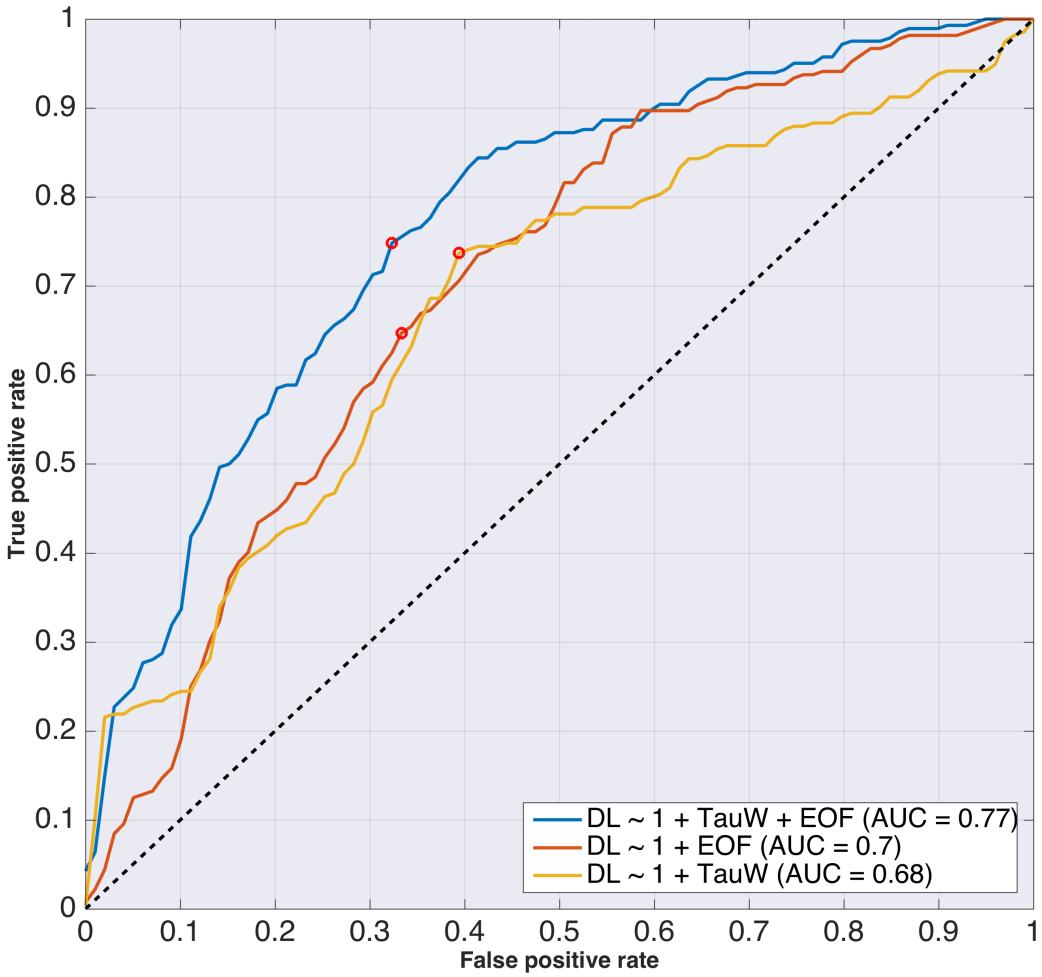

Figure 40. Comparison of logistic regression models computed for τ_w (yellow), M_2 internal-tide (red), and additive combination of the two (blue) using ROC analysis. The optimal operating point of each ROC curve calculated using the ROC cost function are indicated by red dots.

Table 11

Comparison of classification performance via ROC curve optimal operating point

Model	True positive rate	False positive rate	Threshold*	AUC
DL ~ 1 + M_2	64.7%	33.3%	0.46	0.70
DL ~ 1 + τ_{w50m}	73.7%	39.4%	0.39	0.68
DL ~ 1 + τ_{w50m} + M_2	74.8%	32.3%	0.42	0.77

*Optimal operating threshold.

Discussion

Observations of Detached SPM Layers

Throughout the course of the field deployment, we observed numerous accounts of detached SPM layers independent of the surface mixed layer and detached or detaching from the BBL. Concentrations of SPM carried within the mid-water column oscillated on low, 3-7 day, periods with a secondary fluctuation trend dominated by the period of the M_2 internal-tide and were centered ~18 mab, but maxima were seen as high as ~45 mab. Similar observations of fine-grained particles detached from the seafloor have been made over mid or outer continental shelves (Bogucki et al., 1997; Cheriton et al., 2014; Johnson et al., 2001; Klymak et al., 2007; Klymak & Moum, 2003). Of particular relevance are observations from very near to the study site, on the southern Monterey Bay shelf in water depths of 70– 90 m, where Carter et al. (2005) noted acoustic backscatter pulses extending upward from the seafloor to between 20 and 50 mab.

The results from the particle tracking algorithm indicated that detached SPM layers were spatially distributed over the entire shelf along the horizontal principal component of the time-averaged current fields ($\theta = 21^{\circ}$). The results produced under particle tracking algorithm analysis likely suffer from large error margins mainly introduced by two terms: 1) The generalization of current velocities for the entire southern shelf from measurements from a single point (the study site), and 2) The uncertainty in the ADCP measurements of vertical current velocities of ± 0.015 m s^{-1} (equivalent to the mean of maximum vertical current velocities).

While these uncertainties dampen the reliability of the analysis, an interesting result that arises from this exercise is that the majority of the simulated particles remained in suspension throughout the 24 hr period that the model tracked them. These results are an order of a magnitude larger than previous estimates made by Cheriton et al. (2014), which did not account for the influence of vertical current velocities in the mid water column. I have found that during the 2012 study period, the vertical structure of the currents was an important feature for maintaining particles in suspension, especially in mid-water depths where the vertical placement of particles was strongly influenced by what seemed to be periodic upward vertical velocity bursts.

Similar observations of vertical velocity bursts were reported by Cheriton et al. (2014), which concluded that they were important for lifting particles from the BBL to the mid-water column. Others have reported similar upsweeps of fine-grained seafloor particles in the BBL and have associated them with the passage NLIWs on mid or outer continental shelves (Bogucki et al., 1997; Carter et al., 2005; Johnson et al., 2001; Klymak et al., 2007; Klymak & Moum, 2003). My results indicate that in addition to lifting particles from the BBL, vertical velocity bursts are likely important for maintaining particles and flocs suspended in the mid-water column for periods longer than 24 hours; this could allow for greater horizontal advection and distribution of SPM than commonly thought.

Predictors of Detached SPM Layers

As in previous studies, my findings identify surface wave-induced bed shear stresses as the primary control over resuspension of fine particulates in the BBL.

Although SPM concentrations in the BBL at the 70 m study site were decoupled from those seen in the mid-water-column, I have found a time-lagged correlated relationship between SPM found in the BBL at shallower shelf depths (50 m) to the SPM observed in the mid-water column at the 70 m study site. The time-lagged coupling between bed shear stresses at the 50 m isobath and concentrations of SPM in the mid-water column at the 70 m study site was identified by cross-correlation analysis and the logistic regression model selection process. This time-lag reflects the dominant role of advection in determining the timing of detached SPM layers at the 70 m study site. Elevated bed shear stress in shallower depths can be thought of as a first-order requisite for the appearance of detached SPM layers by providing sufficient energy to keep the BBL filled with SPM.

Favorable conditions for detached SPM layers on the Monterey Bay midshelf appear to include not only large enough surface waves for recent seafloor resuspension in the BBL but also energetic internal tides. During the period of observation, variability of SPM by the M_2 frequency was most pronounced during periods of high SPM concentrations and was vertically distributed along the water column in similar patterns as detached SPM layers. The logistic regression model selection process further accentuated the relationship between the M_2 internal-tide and the appearance of detached SPM layers: both AIC and AUC model quality statistics were preeminent for the M_2 internal-tide cross-shore component (u) at a 12-hour lag (~one tidal cycle).

The coupling between the appearance of detached SPM layers and cross-shore component (u) of the M_2 internal-tide is likely the result of the direction of the internal-wave propagation compared to the topographic slope of the southern Monterey Bay shelf.

Under mean summer hydrographic conditions, the shelf is critical to the M_2 internal tide directly upslope from the inshore mud belt boundary (~30–50 m isobaths) (Jachec, 2012). However, the inshore critical slope region likely varies depending on regional hydrography and stratification.

An important finding of this study is that the co-occurrence of the individual physical processes discussed above seems to significantly increase the likelihood of observing detached SPM layers. The results from the logistic regression model that accounted for the additive combination of τ_w computed for the 50 m isobath and the cross-shore (u) component of the M_2 internal-tide outperformed the models computed for each of the predictors individually in its ability to explain the data (e.g., AIC statistic) and its classification capabilities (e.g., Accuracy statistic). The combined logistic regression model clearly shows that observing a detached SPM layer is far more likely when the intensity of both predictors increases.

Wind-Driven Stratification and Energetic Internal Tides

Though we cannot predict the timing of strong internal tide forcing (Nash et al., 2012), evidence presented by Cheriton et al., (2014b) and in this thesis have shown that during the 2012 study period the ability of energetic internal tides to propagate into Monterey Bay appeared to also be, to some extent, connected to wind-driven shifts in stratification over the shelf (Figure 42). During the field experiment, the influx of dense water up onto the shelf provided the stratification necessary to support energetic two-layered internal tides. The evidence presented here support the notion that at this shelf depth, wind-driven variations in bulk hydrographic conditions over the shelf may be just

as important for sediment transport events as the more commonly considered surface swell events that erode the seafloor.

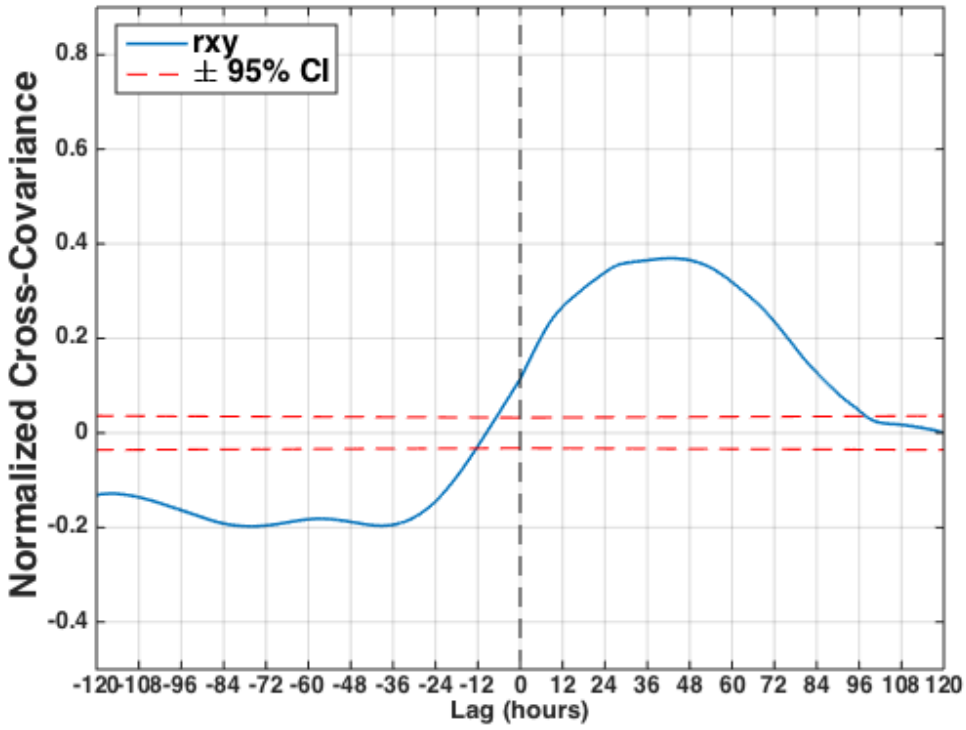

Figure 41. Normalized cross-covariance coefficients illustrating the lagged relationships between wind-driven shifts in isotherm vertical placement over the shelf ($\xi_{12°C}$) and the energy of the cross-shore (u) component of the M_2 internal-tide over the 2012 deployment period. Wind-driven variations in bulk hydrographic conditions are represented by the height above the bottom of the 12°C ($\xi_{12°C}$ low-passed <30hr), which closely followed the near-bottom secondary pycnocline. The strength of the M_2 internal-tide is computed as the 5-day sliding variance of cross-shore current velocity EOF mode 1. The signals are significantly correlated between 12 to ~ 72 hours.

Conclusion

Most studies of the processes controlling suspension and redistribution of particulate matter on continental shelves have focused on SPM transported within the BBL. Studies that have focused on SPM carried in mid-water column over the continental shelf were unable to adequately resolve transport patterns due to temporal or event-scale

variability of benthic-interior exchange processes. This study provided insight about the spatial and temporal variations of SPM transport in mid-water column over the continental shelf and linked changes in oceanographic conditions with vertical advection of sediment beyond the BBL and through the mid-water column.

During the period of observation detached SPM layers oscillated on low, 3-7 day, periods with a secondary fluctuation trend dominated by the period of the M2 internal-tide and were centered ~18 mab. Forcing of detached SPM layers appear to include not only large enough surface waves for recent seafloor resuspension in the BBL but also, and of equal importance, energetic internal tides. A probabilistic model based on co-occurrence of the two environmental processes predicted the appearance of detached SPM layers with 77% accuracy. The ability of energetic internal tides to propagate into Monterey Bay appeared to also be, to some extent, connected to wind-driven shifts in stratification over the shelf.

References

Aghsaee, P., Boegman, L., Diamessis, P. J., & Lamb, K. G. (2012). Boundary-layer-separation-driven vortex shedding beneath internal solitary waves of depression. *Journal of Fluid Mechanics*, *690*, 321–344.

Akaike, H. (1998). Information theory and an extension of the maximum likelihood principle. In *Selected Papers of Hirotugu Akaike* (pp. 199–213). New York, NY, USA: Springer New York.

Azetsu-Scott, K., Johnson, B. D., & Petrie, B. (1995). An intermittent, intermediate nepheloid layer in Emerald Basin, Scotian Shelf. *Continental Shelf Research*, *15*(2), 281–293.

Boegman, L., Ivey, G. N., & Imberger, J. (2005). The degeneration of internal waves in lakes with sloping topography. *Limnology and Oceanography*, *50*(5), 1620–1637.

Bogucki, D., Dickey, T., & Redekopp, L. G. (1997). Sediment resuspension and mixing by resonantly generated internal solitary waves. *Journal of Physical Oceanography*, *27*(7), 1181–1196.

Bourgault, D., Morsilli, M., Richards, C., Neumeier, U., & Kelley, D. E. (2014). Sediment resuspension and nepheloid layers induced by long internal solitary waves shoaling orthogonally on uniform slopes. *Continental Shelf Research*, *72*, 21–33.

Breaker, L. C., & Broenkow, W. W. (1994). The circulation of Monterey Bay and related processes. *Oceanography and Marine Biology*, *32*, 1–64.

Bruland, K. W., Rue, E. L., & Smith, G. J. (2001). Iron and macronutrients in California coastal upwelling regimes: Implications for diatom blooms. *Limnol. Oceanogr*, *46*(7), 1661–1674.

Cacchione, D. A., & Drake, D. E. (1986). Nepheloid layers and internal waves over continental shelves and slopes. *Geo-Marine Letters*, *6*(3), 147–152.

Cacchione, D. A., & Southard, J. B. (1974). Incipient sediment movement by shoaling internal gravity waves. *Journal of Geophysical Research*, *79*(15), 2237–2242.

Carter, G. S., Gregg, M. C., & Lien, R. C. (2005). Internal waves, solitary-like waves, and mixing on the Monterey Bay shelf. *Continental Shelf Research*, *25*(12–13), 1499–1520.

Cazenave, F., Zhang, Y., McPhee-Shaw, E., Bellingham, J. G., & Stanton, T. P. (2011). High-resolution surveys of internal tidal waves in Monterey Bay, California, using an autonomous underwater vehicle. *Limnology and Oceanography: Methods*, *9*(12), 571–581.

Cheriton, O. M., McPhee-Shaw, E. E., Shaw, W. J., Stanton, T. P., Bellingham, J. G., & Storlazzi, C. D. (2014). Suspended particulate layers and internal waves over the southern Monterey Bay continental shelf: An important control on shelf mud belts? *Journal of Geophysical Research: Oceans*, *119*(1), 428–444.

Cheriton, O. M., McPhee-Shaw, E. E., Storlazzi, C. D., Rosenberger, K. J., Shaw, W. J., & Raanan, B. Y. (2014). Upwelling rebound, ephemeral secondary pycnoclines, and the creation of a near-bottom wave guide over the Monterey Bay continental shelf. *Geophysical Research Letters*, *41*(23), 8503–8511.

De Madron, X. D. (1994). Hydrography and nepheloid structures in the Grand-Rhône canyon. *Continental Shelf Research*, *14*(5), 457–477.

Dickson, R. R., & McCave, I. N. (1986). Nepheloid layers on the continental slope west of Porcupine Bank. *Deep Sea Research Part A. Oceanographic Research Papers*, *33*(6), 791–818.

Donelan, M. A., Hamilton, J., & Hui, W. (1985). Directional spectra of wind-generated waves. *Philosophical Transactions of the Royal Society of London A: Mathematical, Physical and Engineering Sciences*, *315*(1534), 509–562.

Dunbar, G. B., & Barrett, P. J. (2005). Estimating palaeobathymetry of wave-graded continental shelves from sediment texture. *Sedimentology*, *52*(2), 253–269.

Edwards, B. D. (2002). Variations in sediment texture on the northern Monterey Bay National Marine Sanctuary continental shelf. *Marine Geology*, *181*(1–3), 83–100.

Eisma, D. (1993). *Suspended matter in the aquatic environment* (1st ed.). Springer-Verlag Berlin Heidelberg. http://doi.org/10.1007/978-3-642-77722-6

Eittreim, S. L., Anima, R. J., & Stevenson, A. J. (2002). Seafloor geology of the Monterey Bay area continental shelf. *Marine Geology*, *181*(1), 3–34.

Ferré, B., Sherwood, C. R., & Wiberg, P. L. (2010). Sediment transport on the Palos Verdes shelf, California. *Continental Shelf Research*, *30*(7), 761–780.

Gardner, W. D. (1989). Periodic resuspension in Baltimore Canyon by focusing of internal waves. *Journal of Geophysical Research: Oceans*, *94*(C12), 18185–18194.

Gelman, A., & Hill, J. (2006). *Data analysis using regression and multilevel/hierarchical models*. New York, NY, USA: Cambridge University Press.

George, D. A., & Hill, P. S. (2008). Wave climate, sediment supply and the depth of the sand–mud transition: a global survey. *Marine Geology*, *254*(3), 121–128.

Glover, D. M., Jenkins, W. J., & Doney, S. C. (2011). *Modeling methods for marine science*. Cambridge, UK: Cambridge University Press.

Grant, W. D., & Madsen, O. S. (1979). Combined wave and current interaction with a rough bottom. *Journal of Geophysical Research: Oceans*, *84*(C4), 1797–1808.

Harris, C. K., & Wiberg, P. L. (2001). A two-dimensional, time-dependent model of suspended sediment transport and bed reworking for continental shelves. *Computers and Geosciences*, *27*(6), 675–690.

Helfrich, K. R. (1992). Internal solitary wave breaking and run-up on a uniform slope. *Journal of Fluid Mechanics*, *243*, 133–154.

Hosegood, P., Bonnin, J., & van Haren, H. (2004). Solibore-induced sediment resuspension in the Faeroe-Shetland channel. *Geophysical Research Letters*, *31*(9), 2–5.

Inthorn, M., Mohrholz, V., & Zabel, M. (2006). Nepheloid layer distribution in the Benguela upwelling area offshore Namibia. *Deep Sea Research Part I: Oceanographic Research Papers*, *53*(8), 1423–1438.

Jachec, S. M. (2012). Power estimates associated with internal tides from the Monterey Bay area. *Oceanography*, *25*(2), 52–55.

Jachec, S. M., Fringer, O. B., Gerritsen, M. G., & Street, R. L. (2006). Numerical simulation of internal tides and the resulting energetics within Monterey Bay and the surrounding area. *Geophysical Research Letters*, *33*(12).

Johnson, D. R., Weidemann, A., & Pegau, W. S. (2001). Internal tidal bores and bottom nepheloid layers. *Continental Shelf Research*, *21*(13), 1473–1484.

Key, S. A. (1999). *Internal tidal bores in the Monterey Canyon.* Naval Postgrad. Sch., Monterey, Calif.

Klymak, J. M., & Moum, J. N. (2003). Internal solitary waves of elevation advancing on a shoaling shelf. *Geophysical Research Letters*, *30*(20), 2045–2049.

Klymak, J. M., Moum, J. N., Nash, J. D., Perlin, A., & Smyth, W. D. (2007). Energy Transport by Nonlinear Internal Waves. *Journal of Physical Oceanography*, *37*(7), 1968–1988.

Krusche, J. (2010). Doing Bayesian data analysis: a tutorial introduction with R. Academic Press.

Lucas, A. J., Franks, P. J. S., & Dupont, C. L. (2011). Horizontal internal-tide fluxes support elevated phytoplankton productivity over the inner continental shelf. *Limnology & Oceanography: Fluids & Environments*, *1*, 56–74.

Macskassy, S., & Provost, F. (2004). Confidence bands for ROC curves: Methods and an empirical study. Proceedings of the First Workshop on ROC Analysis in AI. August 2004.

Madsen, O. S. (1994). Spectral Wave-Current Bottom Boundary Layer Flows. *Coastal Engineering Proceedings*, *1*(24), 384–398.

McPhee-Shaw, E. (2006). Boundary-interior exchange: Reviewing the idea that internal-wave mixing enhances lateral dispersal near continental margins. *Deep-Sea Research Part II: Topical Studies in Oceanography*, *53*(1–2), 42–59.

McPhee-Shaw, E. E. (2002). Boundary layer intrusions from a sloping bottom: A mechanism for generating intermediate nepheloid layers. *Journal of Geophysical Research*, *107*, 1–16.

McPhee-Shaw, E. E., Sternberg, R. W., Mullenbach, B., & Ogston, A. S. (2004). Observations of intermediate nepheloid layers on the northern California continental margin. *Continental Shelf Research*, *24*(6), 693–720.

Nash, J. D., Shroyer, E., Kelly, S. M., Inall, M. E., Duda, T. F., Levine, M., … Musgrave, R. (2012). Are Any Coastal Internal Tides Predictable? *Oceanography*, *25*(2), 80–95.

Nédélec, F., Statham, P. J., & Mowlem, M. (2007). Reprint of "Processes influencing

dissolved iron distributions below the surface at the Atlantic Ocean–Celtic Sea shelf edge." *Marine Chemistry*, *106*(1), 365–379.

Nielsen, P. (1992). *Coastal bottom boundary layers and sediment transport* (Vol. 4). World scientific.

Nittrouer, C. A., & Wright, L. D. (1994). Transport of particles across continental shelves. *Reviews of Geophysics*, *32*(1), 85–113.

Noble, M. A., & Xu, J. P. (2003). Observations of large-amplitude cross-shore internal bores near the shelf break, Santa Monica Bay, CA. *Marine Environmental Research*, *56*(1), 127–149.

Ogston, A. S., & Sternberg, R. W. (1999). Sediment-transport events on the northern California continental shelf. *Marine Geology*, *154*(1–4), 69–82.

Pak, H., Zaneveld, J. R., & Kitchen, J. (1980). Intermediate nepheloid layers observed off Oregon and Washington. *Journal of Geophysical Research*, *Vol. 85*(C11), 6697–6708.

Pawlowicz, R., Beardsley, B., & Lentz, S. (2002). Classical tidal harmonic analysis including error estimates in MATLAB using T_TIDE. *Computers & Geosciences*, *28*(8), 929–937.

Petruncio, E. T. (1993). *Characterization of tidal currents in Monterey Bay from remote and in-situ measurements*. Naval Postgraduate School, Monterey, California.

Petruncio, E. T., Rosenfeld, L. K., & Paduan, J. D. (1998). Observations of the internal tide in Monterey Canyon. *Journal of Physical Oceanography*, *28*(10), 1873–1903.

Puig, P. (2004). Role of internal waves in the generation of nepheloid layers on the northwestern Alboran slope: Implications for continental margin shaping. *Journal of Geophysical Research*, *109*(C9), C09011.

Rosenfeld, L. K., Schwing, F. B., Garfield, N., & Tracy, D. E. (1994). Bifurcated flow from an upwelling center: a cold water source for Monterey Bay. *Continental Shelf Research*, *14*(9), 931–964.

Ryan, J. P., Chavez, F. P., & Bellingham, J. G. (2005). Physical-biological coupling in Monterey Bay, California: Topographic influences on phytoplankton ecology. *Marine Ecology Progress Series*, *287*, 23–32.

Sevadjian, J. C., McPhee-Shaw, E. E., Raanan, B. Y., Cheriton, O. M., & Storlazzi, C. D. (2015). Vertical convergence of resuspended sediment and subducted phytoplankton to a persistent detached layer over the southern shelf of Monterey Bay, California. *Journal of Geophysical Research: Oceans*, *120*(5), 3462–3483.

Soulsby, R. (1997). *Dynamics of marine sands: a manual for practical applications*. Thomas Telford.

Stanton, T. P., & Ostrovsky, L. A. (1998). Observations of highly nonlinear internal solitons over the continental shelf. *Geophysical Research Letters*, *25*(14), 2695–2698.

Sternberg, R. W., Berhane, I., & Ogston, A. S. (1999). Measurement of size and settling velocity of suspended aggregates on the northern California continental shelf. *Marine Geology*, *154*(1–4), 43–53.

Sternberg, R. W., & Larsen, L. H. (1975). Threshold of sediment movement by open ocean waves: observations. *Deep-Sea Research and Oceanographic Abstracts*, *22*(5).

Stokes, G. G. (1851). *On the effect of the internal friction of fluids on the motion of pendulums* (Vol. 9). Pitt Press.

Storlazzi, C. D., McManus, M. A., & Figurski, J. D. (2003). Long-term, high-frequency current and temperature measurements along central California: insights into upwelling/relaxation and internal waves on the inner shelf. *Continental Shelf Research*, *23*(9), 901–918.

Storlazzi, C. D., Reid, J. A., & Golden, N. E. (2007). *Wave-driven spatial and temporal variability in sea-floor sediment mobility in the Monterey Bay, Cordell Bank, and Gulf of the Farallones National Marine Sanctuaries*. US Geological Survey.

Sullivan, J. M., Donaghay, P. L., & Rines, J. E. B. (2010). Coastal thin layer dynamics: Consequences to biology and optics. *Continental Shelf Research*, *30*(1), 50–65.

Syvitski, J. P., & Morehead, M. D. (1999). Estimating river-sediment discharge to the ocean: application to the Eel margin, northern California. *Marine Geology*, *154*(1), 13–28.

Thomson, R. E., & Emery, W. J. (2014). *Data analysis methods in physical oceanography*. Newnes.

Thorpe, S. A., & White, M. (1988). A deep intermediate nepheloid layer. *Deep Sea Research Part A. Oceanographic Research Papers*, *35*(9), 1665–1671.

Venayagamoorthy, S. K., & Fringer, O. B. (2007). On the formation and propagation of nonlinear internal boluses across a shelf break. *Journal of Fluid Mechanics*, *577*, 137–159.

Walter, R. K., Brock Woodson, C., Arthur, R. S., Fringer, O. B., & Monismith, S. G. (2012). Nearshore internal bores and turbulent mixing in southern Monterey Bay. *Journal of Geophysical Research: Oceans*, *117*(7), 1–13.

Wang, X., Chao, Y., Dong, C., Farrara, J., Li, Z., McWilliams, J. C., … Rosenfeld, L. K. (2009). Modeling tides in Monterey Bay, California. *Deep-Sea Research Part II: Topical Studies in Oceanography*, *56*(3–5), 219–231.

Weering, T. C. E. Van, Stigter, H. C. De, Balzer, W., Epping, E. H. G., Graf, G., Hall, I. R., … Vangriesheim, A. (2001). Benthic dynamics and carbon fluxes on the NW European continental margin, *48*, 3191–3221.

Wiberg, P. L., & Sherwood, C. R. (2008). Calculating wave-generated bottom orbital velocities from surface-wave parameters. *Computers and Geosciences*, *34*(10), 1243–1262.

Woodson, C. B., Barth, J. A., Cheriton, O. M., McManus, M. A., Ryan, J. P., Washburn, L., … Garske, L. E. (2011). Observations of internal wave packets propagating along-shelf in northern Monterey Bay. *Geophysical Research Letters*, *38*(1).

Appendix A

Beckman Coulter LS Particle Size Analyzer result sheet

Beckman Coulter LS Particle Size Analyzer

22 Mar 2013 14:43

File name: C:\Particle Size Data\Classes\cOASTALdYN2013\SG6_10_29_b_5212_01.$ls
File ID: SG6_10_29_b
Run number: 5212
Optical model: Fraunhofer.rfd PIDS included
LS 13 320 Aqueous Liquid Module

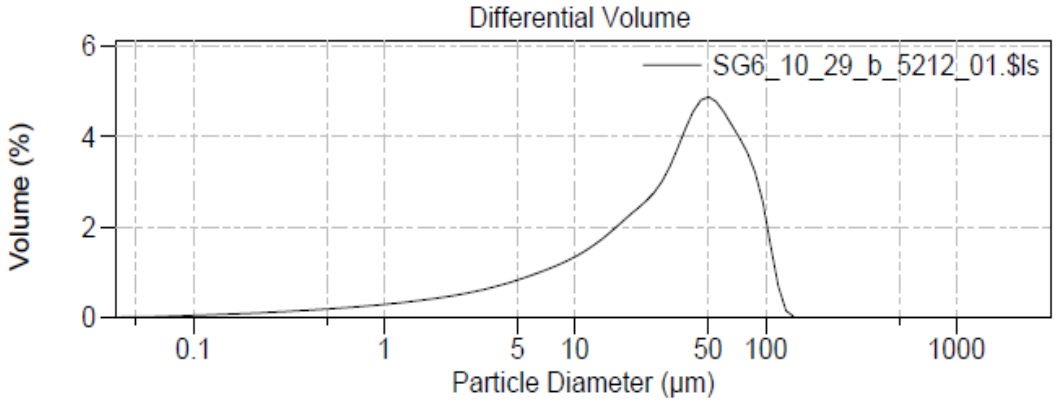

Volume Statistics (Geometric) SG6_10_29_b_5212_01.$ls

Calculations from 0.0400 µm to 2000 µm

Volume:	100%		
Mean:	23.29 µm	S.D.:	3.628
Median:	34.45 µm	Variance:	13.16
D(3,2):	5.445 µm	Skewness:	-1.489 Left skewed
Mean/Median ratio:	0.676	Kurtosis:	2.262 Leptokurtic
Mode:	50.22 µm		
d_{10}:	3.825 µm		
d_{50}:	34.45 µm		
d_{90}:	80.33 µm		
Specific Surf. Area:	11020 cm^2/mL		

% <	10	25	50	75	90
µm	3.825	13.60	34.45	57.44	80.33

Beckman Coulter LS Particle Size Analyzer

Page 2
22 Mar 2013 14:43

SG6_10_29_b_5212_01.$ls

Particle Diameter µm	Volume % <
4	10.3281
6	13.8633
10	20.0197
32	47.1816
63	79.5193
125	99.8799
250	100
500	100

Appendix B

Vertical profiles of time-domain EOF analysis for ADCP currents

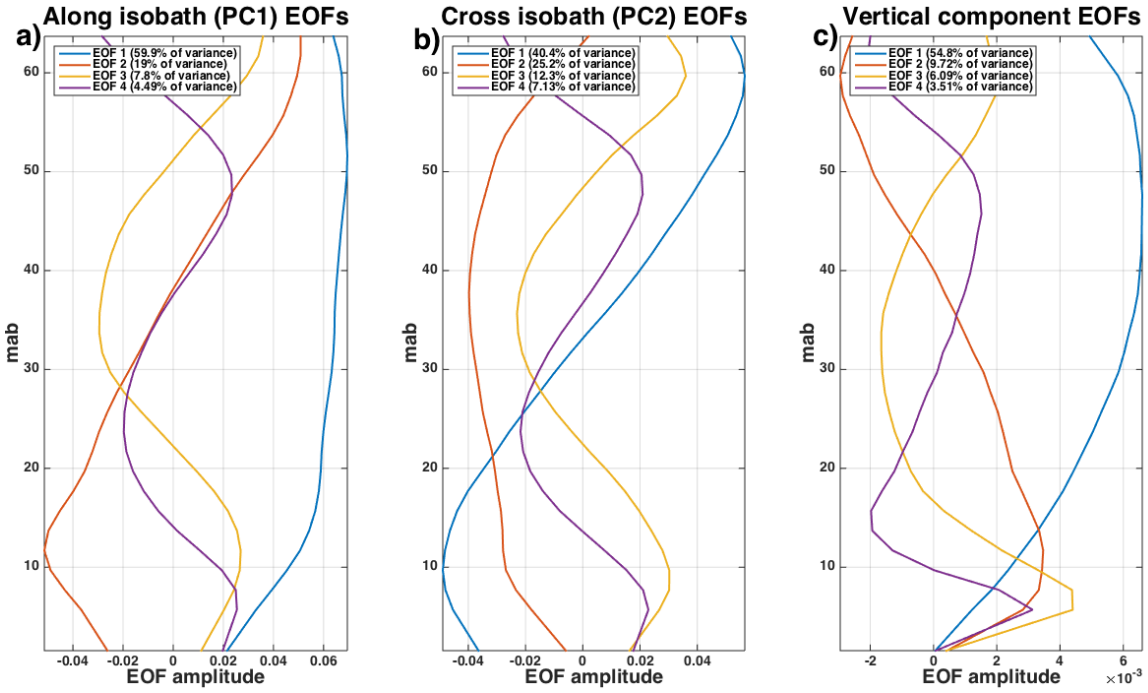

Appendix C

Variance preserving spectral density of time-domain EOF components

decomposed from along-shore (a-b), cross-shore (c-d) and vertical (e-f) ADCP currents